Dual-plane stereo particle image velocimetry measurements of velocity gradient tensor fields in turbulent shear flow. I. Accuracy assessments

John A. Mullin and Werner J. A. Dahm[a)]
Laboratory for Turbulence & Combustion (LTC), Department of Aerospace Engineering, The University of Michigan, Ann Arbor, Michigan 48109-2140

(Received 22 July 2004; accepted 22 September 2005; published online 9 March 2006)

Results are presented from quantitative assessments of the accuracy of velocity gradients measured by a dual-plane stereo particle image velocimetry (DSPIV) technique that allows direct, highly resolved, nonintrusive measurements of all nine simultaneous components of the velocity gradient tensor fields $\partial u_i/\partial x_j$ at the quasi-universal intermediate and small scales of turbulent shear flows. The present results systematically determine the sources of errors in DSPIV measurements and the resulting accuracy of velocity gradients obtained from such measurements. Intrinsic errors resulting from asymmetric stereo imaging are found by synthetic particle imaging to be no larger than 0.8%. True particle imaging in finite-thickness light sheets is found from single-plane imaging tests to produce net errors in measured velocity differences of 6% for in-plane components and 10% for out-of-plane components. Further errors from limits on the accuracy of independent dual light sheet generation and positioning are found from coincident-plane imaging tests to produce overall errors of 9% and 16% in the in-plane and out-of-plane velocity differences. Practical DSPIV velocity gradient component measurements are found from separated-plane imaging tests in a turbulent shear flow to show excellent similarity in on-diagonal ($i=j$) and off-diagonal ($i\neq j$) components of $\partial u_i/\partial x_j$, as well as mean-square gradient values showing agreement within 1%–4% of ideal isotropic limit values. The resulting measured divergence values are consistent with overall rms errors obtained from the coincident-plane imaging tests. Collectively, these results establish the accuracy with which all nine simultaneous components of the velocity gradient tensor fields $\partial u_i/\partial x_j$ can be obtained from DSPIV measurements at the quasi-universal intermediate and small scales of turbulent shear flows. © *2006 American Institute of Physics*. [DOI: 10.1063/1.2166447]

I. INTRODUCTION

A significantly improved understanding of turbulence in shear flows, and corresponding development of subgrid-scale models for large-eddy simulations of such flows, will likely require improved access to the physical structure and dynamics of the intermediate and small scales of high Reynolds number turbulent shear flows. Key interest is in the structure, statistics, similarity, and scaling properties of these quasi-universal scales in shear flows under various conditions. These issues are of particular importance for quantities such as the strain rate and vorticity fields, the kinetic energy dissipation rate field, and other gradient fields derived from the velocity derivatives.[1] To date, due to the difficulty in accurately measuring all nine simultaneous components of the velocity gradient tensor field at the intermediate and small scales of turbulent flows, these quantities have been primarily studied by direct numerical simulation (DNS). That approach has been particularly successful in homogeneous isotropic or uniformly sheared turbulence in periodic domains, for which the computational requirements are relatively manageable. However, comparable DNS studies of spatially developing turbulent shear flows are typically confined to relatively low Reynolds numbers, due to the computational burden of resolving the full range of inner and outer flow scales over a sufficiently large downstream extent for the flow to achieve its fully developed state. At the same time, new multidimensional measurement techniques are now providing experimental access to flow information that had previously been accessible only by simulations. Such experimental measurements may provide the most practical way to obtained the detailed structure, statistics, similarity and scaling properties of gradient quantities in turbulent shear flows at a level of resolution and detail that has traditionally been associated only with direct numerical simulation.

Early experimental investigations of velocity gradients in fully developed turbulent flows used single-point time-series data from hot-wire measurements with Taylor's hypothesis to approximate a single component of the velocity gradient tensor.[2] Subsequent studies have developed and applied increasingly capable multiple-wire probes to simultaneously measure several components of the velocity gradient tensor.[3–7] A few studies have used probes with up to 20 hot wires to measure all nine components of the velocity gradient tensor at a single point.[8,9]

More recently, various multidimensional imaging approaches have been developed to allow measurement of velocity gradient fields in shear flow turbulence. Particle image velocimetry (PIV) allows simultaneous nonintrusive measurement of two in-plane velocity components, which provides access to four of the nine velocity gradient tensor com-

a)Author to whom correspondence should be addressed. Electronic mail: wdahm@umich.edu

ponents $\partial u_i/\partial x_j$. These permit formation of three of the six components of the strain rate tensor and a single vorticity component. Stereo PIV, dual-plane PIV, and scanning PIV further provide the out-of-plane velocity component and thereby give access to two further velocity gradient components, however these do not provide any additional components of either the strain rate or the vorticity. Particle tracking velocimetry (PTV) provides three-component velocity fields throughout a three-dimensional volume, and thereby gives access to all nine components of $\partial u_i/\partial x_j$, but the large particle separations needed for accurate tracking prevents velocity gradient measurements at the small scales of turbulence. The most extensive velocity gradient measurements in turbulent flows to date[10] have come from holographic particle image velocimetry (HPIV), though the resolution in those measurements is significantly larger than the smallest scales in the turbulent flow. Velocity gradient measurements have also been reported from scanning stereo PIV in a relatively low Reynolds number turbulent shear flow.[11] Indirect measurements of $\partial u_i/\partial x_j$ via scalar imaging velocimetry (SIV) are based on three-dimensional laser-induced fluorescence imaging of a scalar field and inversion of the conserved scalar transport equation to obtain the underlying three-component velocity field. This has allowed highly resolved measurements of all nine simultaneous components of the velocity gradients at the intermediate and small scales of a turbulent flow,[12–14] but requires smoothness and continuity constraints in the inversion to obtain the velocity field data.

Dual-plane stereo particle image velocimetry (DSPIV) is based on two separate stereo PIV measurements that provide all three components of velocity in two parallel light-sheet planes. This requires separating the light scattered by particles in the two light-sheet planes onto two independent stereo camera pairs. Reference 15 first introduced a polarization-based approach, in which the two light sheets were arranged with orthogonal polarizations so that each stereo camera pair saw the scattered light from only one of the sheets. Such an approach allows all nine components of $\partial u_i/\partial x_j$ to be calculated from the measured velocities in the two planes, with the resolution determined largely by the thickness and spacing of the light-sheet planes and the size of the correlation window in the PIV processing. References 16 and 17 used this to measure comparatively large scale features of the flow in a turbulent boundary layer, and Ref. 18 used the same technique to investigate large-scale features of a lobed jet mixer. Reference 19 has used a related polarization-based dual-plane approach that combines stereo PIV and conventional PIV measurements, with continuity used to estimate the out-of-plane gradient component, to study features of a turbulent boundary layer flow. These studies all investigated specific aspects of these two flows, and did not seek to resolve or study velocity gradients on the quasi-universal intermediate and small scales of turbulent shear flows. Moreover, maintaining the orthogonal polarization in the Mie scattered light required the scattering particles to be spherical, and as a consequence those studies used fine liquid droplets as seed particles. While this can be done in nonreacting turbulent flows, in exothermic reacting flows such liquid droplets do not survive.

References 20–22 introduced a two-frequency DSPIV approach that allows traditional solid metal oxide particles to be used as the seed, thereby permitting measurements in reacting as well as nonreacting turbulent flows. That approach is based on measurements in two differentially spaced light-sheet planes, using two different laser frequencies in conjunction with filters to separate the light scattered from the seed particles onto the individual stereo camera pairs. Moreover, the differential spacing of the two stereo PIV planes allows resolution of all nine components of the $\partial u_i/\partial x_j$ fields down to the local inner (viscous) scale of the turbulent flow, permitting highly resolved experimental studies of the quasi-universal intermediate and small scales of turbulent shear flows.

In this paper, results are presented from rigorous quantitative assessments for the accuracy of velocity gradient component fields obtained from such high-resolution DSPIV measurements in a turbulent shear flow. These assessments systematically identify and quantify a progressively increasing number of the individual error sources that collectively determine the overall accuracy of the $\partial u_i/\partial x_j$ fields obtained with this DSPIV approach. A companion paper[23] presents results from such highly resolved DSPIV measurements in a turbulent shear flow at outer-scale Reynolds numbers up to 30,000 to investigate aspects of the structure, statistics, similarity, and scaling of gradient fields, including the strain rate, vorticity, and kinetic energy dissipation rate, in a turbulent shear flow at differing combinations of the Reynolds number Re_δ and the mean shear rate S.

II. DUAL-PLANE STEREO PIV (DSPIV)

Reference 22 gives a detailed description of the two-frequency dual-plane stereo PIV technique. This section summarizes only those aspects that are relevant to the accuracy of velocity gradients obtained with this technique in turbulent shear flows. As indicated in Figs. 1 and 2, frequency-based DSPIV is based on two simultaneous, independent stereo PIV measurements in two differentially spaced light-sheet planes. This approach uses two different light-sheet frequencies in conjunction with appropriate optical filters to separate the scattered light from particles seeded in the flow onto two independent stereo PIV camera pairs. The present system consists of four Nd:YAG lasers, of which two are sequentially triggered to create the double pulses for the 532 nm light sheets and the other two, also sequentially triggered at the same two instants of time, pump two pulsed dye lasers that provide the 635 nm light sheets. A method based on traversing a knife edge across each sheet and collecting the transmitted light onto a photodiode detector was used to quantitatively establish the 400 ± 20 μm thicknesses of the two 532 nm light sheets and the 800 ± 20 μm thicknesses of the two 635 nm light sheets. An optical technique that images each sheet cross section and determines the sheet centerline based on the measured intensity profiles at various elevations throughout the sheet was used to quantitatively verify coincidence and parallelism, to within less than 1°, of the two 532 and 635 nm light-sheet pairs, and to confirm the 400 ± 20 μm separation between the sheets.[22]

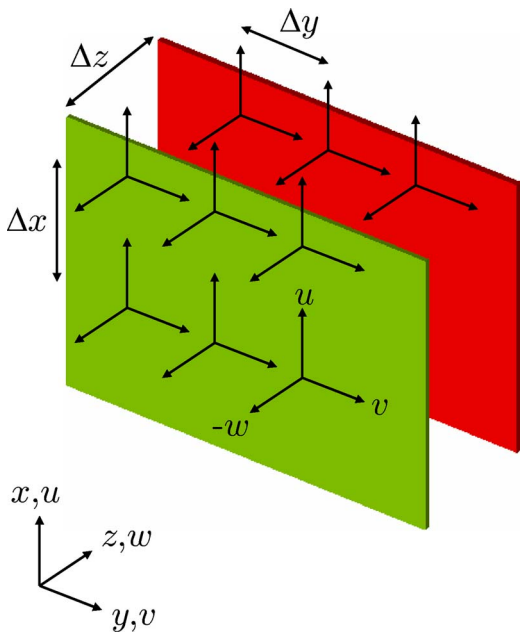

FIG. 1. (Color online) Basic principle for frequency-based dual-plane stereo particle image velocimetry (DSPIV), consisting of two simultaneous independent stereo PIV measurements of all three velocity component fields (u,v,w) in two differentially spaced parallel light sheets, one at 532 nm (green) and one at 635 nm (red). Filters separate light scattered from seed particles onto individual stereo camera pairs in Fig. 2.

The scattered light from 0.5 μm aluminum oxide seed particles is recorded on four 12-bit 1280×1024-pixel interline transfer CCD cameras with 200 ns interframe timing. The field of view is 15.5 mm$\times$12.5 mm, giving a magnification of 0.55 based on the physical size of the CCD chip (8.6 mm$\times$6.8 mm). Each camera uses a Sigma 70-300f/4-5.6 APO macro lens to achieve the desired field of view. The 532 nm camera pair has narrow-band filters centered at 532±5 nm that block the 635 nm light, and the 635 nm cameras are equipped with OG570 Schott glass filters that block the 532 nm light.

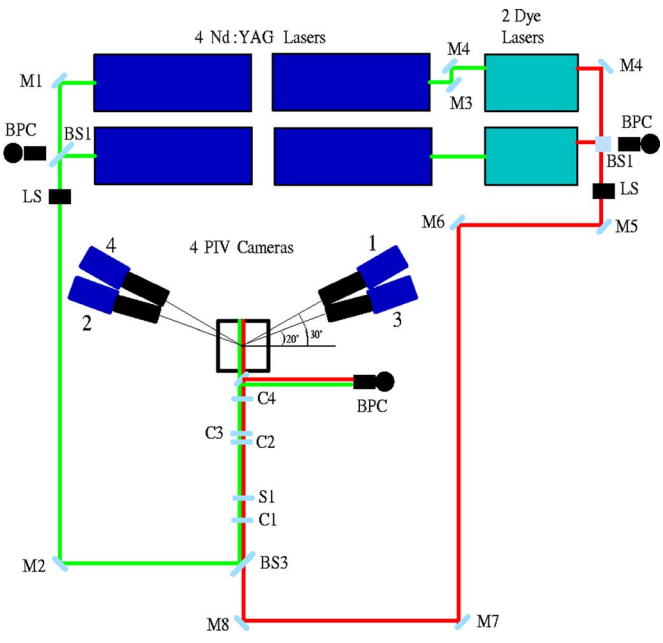

FIG. 2. (Color online) Layout of present frequency-based DSPIV system. Two Nd:YAG lasers provide green light sheets and two Nd:YAG lasers pump two dye lasers providing red light sheets. Two pairs of independent stereo PIV cameras (1–2 and 3–4) are arranged in asymmetric forward-forward scatter configuration. Optical components denoted M# for mirrors, BS# for beamsplitters, LS for laser shutters, C# for cylindrical lenses, and S# for spherical lenses.

The four cameras are arranged in an asymmetric angular-displacement configuration, shown in Fig. 2, with each of the camera pairs satisfying the Scheimpflug condition for stereoscopic imaging. The small field of view of the measurements, coupled with the long focal length of the camera lens, dictates that a large $f\#$ aperture must be used to obtain particle images that are sufficiently focused across the entire field of view. To obtain precise alignment between the object, lens, and image planes while maintaining a coincident field of view for all four cameras, specially designed camera mounts are attached to rails providing forward-backward and side-to-side adjustments, along with fine vertical adjustment and a smooth angular adjustment. In the present camera configuration, each pair of stereo cameras is orientated with an included angle of 50° between the optical axes of each camera pair. System performance studies of such angular-displacement stereo PIV systems[24,25] show that the minimum out-of-plane displacement errors occur at an included angle of 90°, while the minimum in-plane displacement errors occur at an included angle of 0°. Previous studies[26] for asymmetric camera configurations indicate that, for the present 50° included angle and 10° asymmetry angle in Fig. 2, the error ratio is expected to be approximately 1 to 2.

Particle images are processed with an adaptive multipass technique using 32×32 pixel interrogation boxes with no overlap in the final vector fields, giving the same in-plane resolution between vectors as the out-of-plane resolution between the planes. Velocity gradients are computed using linear central differencing in the x and y directions and one-sided differencing in the z direction of the measured velocity fields to obtain all nine components of $\partial u_i/\partial x_j$. The overall spatial resolution in the resulting velocity gradient fields is determined by the collective effects of the laser sheet thicknesses and separation and the PIV processing to be 1100 μm.[22]

III. INTRINSIC DSPIV ACCURACY LIMITS

Fundamental limits on the accuracy of the velocity gradient fields from such DSPIV measurements are obtained by imaging a two-dimensional target of synthetically generated particle images subjected to imposed displacements. The target, consisting of a 35 mm film negative with particle images having the same 0.5 μm particle diameter as the actual seed particles, was displaced with a three-axis set of precision micrometer-controlled translation stages with a position uncertainty of 1.5 μm. After an initial particle image was acquired by both stereo camera pairs, the target was displaced 100 μm along each of the three axes and a second particle image acquired. Variations in the resulting inferred velocity

TABLE I. Rms errors in each velocity component from synthetic particle imaging.

Velocity component	$(u_i)_{\text{rms}}$ (m/s) 532 nm	$(u_i)_{\text{rms}}$ (m/s) 635 nm	$(\Delta u_i)_{\text{rms}}$ (m/s) 532–635
u	0.006	0.004	0.003
v	0.004	0.004	0.003
w	0.008	0.008	0.005
Error ratio	1.8	2.0	

field provide ideal intrinsic limits on the accuracy of DSPIV measurements.

Table I gives results for the rms variations in the velocity components within each camera-pair plane and between the two camera-pair planes. The rms errors in the out-of-plane (w) velocity component are significantly larger than for the two in-plane (u and v) components. The standard "error ratio," defined as the ratio of rms errors in the out-of-plane and in-plane velocity components, gives values of 1.8 and 2.0 for the two independent stereo camera pairs. Table I indicates that rms errors in the velocity differences between the two independent stereo measurements, which are central to determining velocity gradients from the measured velocities, are no larger than 0.8%.

Simulations are typically used to assess the effects of various additional parameters on the accuracy of the resulting velocity fields,[27,28] including particle diameter, displacement, number density, image discretization, background noise, and displacement gradients across the interrogation region. Based on these, expected values for various contributing error sources were generated for conditions applicable to the present DSPIV system, corresponding to a particle diameter of 2 pixels, a 32×32 pixel interrogation box, and a maximum particle displacement of 8 pixels. The combined effects indicate a net bias error of −0.035 pixels and a net rms error of +0.145 pixels, giving a total error of +0.110 pixels. For the 8-pixel particle displacement this corresponds to a net error of +1.4% in the resulting velocity components. Additionally, theoretical error analyses for symmetric[25] and asymmetric[26] stereo imaging configurations indicate that the present DSPIV system configuration should have rms errors of approximately 1%–2% in the in-plane velocity components and 3%–4% in the out-of-plane components. It will be seen in Secs. IV and V that these estimates are consistent with experimentally measured values for the present system.

IV. SINGLE-PLANE DSPIV IMAGING ASSESSMENTS

A direct assessment of the accuracy of velocity gradient measurements with DSPIV can be obtained from tests based on single-plane imaging. In such tests, both stereo camera pairs in the DSPIV system are arranged to image the same particle field in the same double-pulsed light sheet. In principle, the velocity fields resulting from the two camera pairs should then be identical. Differences in the two independently measured velocity fields thus allow quantitative determination of the accuracy with which velocity gradients can be measured.

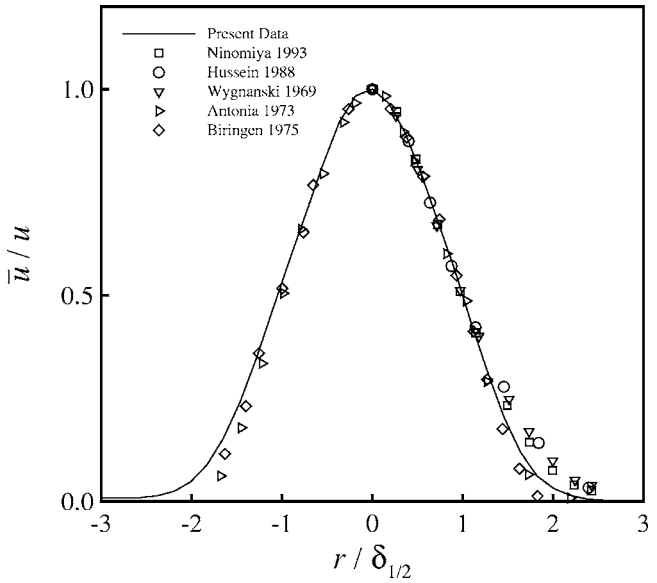

FIG. 3. Measured mean streamwise velocity component $u\equiv U-U_\infty$ in the coflowing turbulent jet used in present DSPIV imaging assessments.

A. Flow configuration

Such single-plane imaging assessments were made on the centerline in the self-similar far field of an axisymmetric coflowing turbulent jet. Details of the flow facility are given in Ref. 29. Air seeded with 0.5 μm aluminum oxide particles issued from a 1.0 m long tube with 2.2 mm inner diameter at nominal exit velocity $U_o=12.7$ m/s into a uniformly seeded coflowing air stream in a 30×30 cm test section at coflow velocity $U_\infty=0.25$ m/s. Measurements were made 17 cm downstream of the nozzle exit, corresponding to $(x/\vartheta)=2.1$, where ϑ is the invariant momentum radius of the flow. This (x/ϑ) value is within the jet-like scaling limit of the coflowing jet.[30,31] In coflowing jets, the excess velocity $u\equiv U-U_\infty$ determines the local shear. For the present conditions, the local mean centerline velocity $u_c=1.2$ m/s and local flow width $\delta=7.5$ cm give the local outer-scale Reynolds number $\text{Re}_\delta=6{,}000$. Conventional PIV measurements of the resulting mean velocity profile in Fig. 3 and the corresponding velocity fluctuation profiles in Fig. 4 show good agreement with previously reported results[32–34] and serve to validate the turbulent shear flow used in these tests. At these conditions, the 1100 μm overall resolution of the DSPIV measurements corresponds to 0.89 viscous length scales λ_ν, equivalent to about 5 Kolmogorov length scales λ_K.

B. Velocity differences

Typical results for the two independently measured velocity fields $\mathbf{u}(\mathbf{x},t)$ from single-plane imaging assessments of the present DSPIV system in this flow configuration are given in Figs. 5 and 6. It is apparent in Fig. 5 that the two velocity fields are very nearly identical. Figure 6 thus shows the individual instantaneous velocity component fields

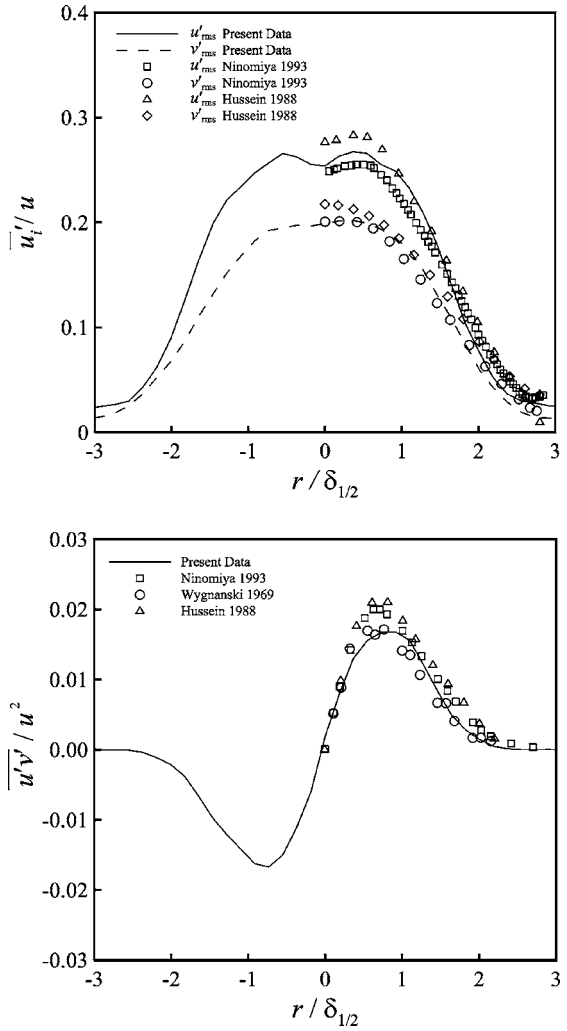

FIG. 4. Measured radial profiles of streamwise (u'_{rms}) and radial (v'_{rms}) rms velocity fluctuations (top) and Reynolds stress profile $\overline{u'v'}$ (bottom), for flow configuration used in present DSPIV imaging assessments.

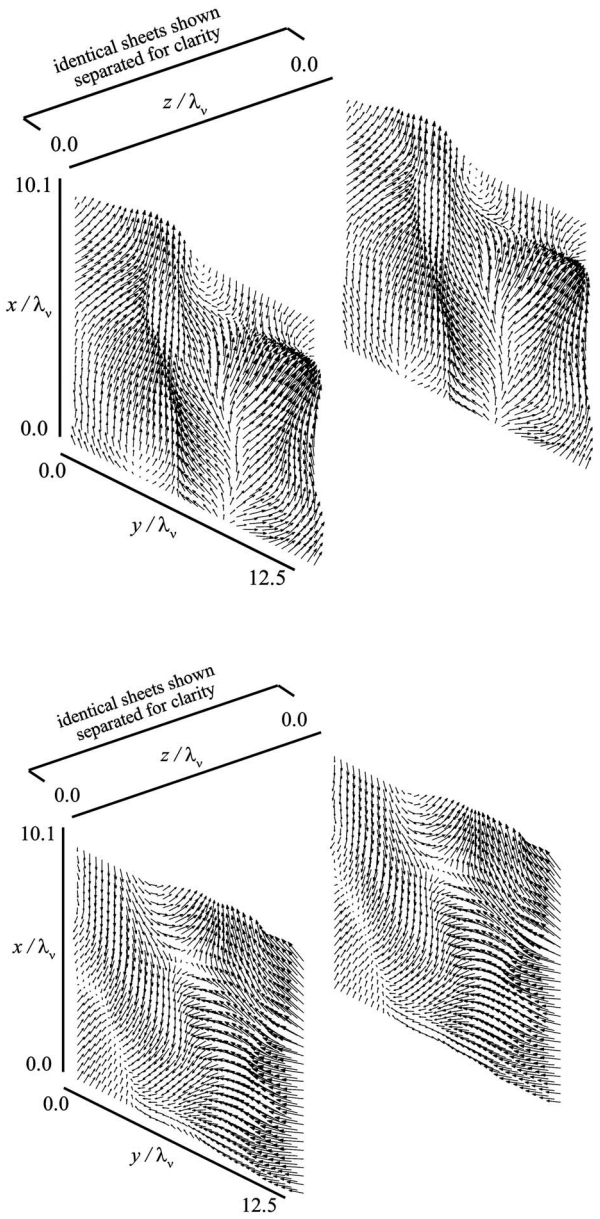

FIG. 5. Two typical instantaneous velocity vector fields $\mathbf{u}(\mathbf{x},t)$ from single-plane DSPIV imaging assessments, showing independently measured fields from both stereo camera pairs. Mean velocity has been subtracted and planes are shown separated to allow clearer comparisons.

$u_i(\mathbf{x},t)$, obtained from the two independent stereo camera pairs as both image particles in the same 532 nm light sheet, together with the corresponding differences $\Delta u_i(\mathbf{x},t)$ between the resulting component fields in the rightmost column on the same quantitative color scale. The differences Δu_i in the two velocity component measurements can be seen to be far smaller than the velocity component values themselves, reflecting the comparatively high accuracy of these measurements. It is also apparent that the w-component differences are typically larger than the u- and v-component differences, consistent with the results in Table I, due to the inherently higher error in measuring the out-of-plane velocity component with stereo PIV systems.

Probability densities of the independently measured velocity components u_i, together with the respective differences Δu_i, are shown on the same scale in Fig. 7. There are two curves shown in each of the $P(u_i)$ distributions, one resulting from each independent stereo camera pair. The velocity component distributions from the two stereo camera pairs are virtually identical, and by comparing with the velocity difference distributions $P(\Delta u_i)$ it is apparent that the measurement errors $\Delta u_i \ll u_i$. Table II gives the resulting rms values of u_i and Δu_i. The typical relative errors in the velocity differences are seen to be no more than 6.5% for the in-plane components and 10.5% for the out-of-plane components.

C. Velocity gradients

Figures 8 and 9 show comparisons of the six measured velocity gradient component fields $\partial u_i/\partial x$ and $\partial u_i/\partial y$ accessible by such single-plane imaging assessments, obtained independently from each of the two stereo camera pairs. It is apparent that the resulting velocity gradients are nearly the same from both camera pairs, further verifying the accuracy of velocity gradient fields from DSPIV measurements. Probability densities for the velocity gradient components are presented in Fig. 10 in linear axes and in Fig. 11 in semi-

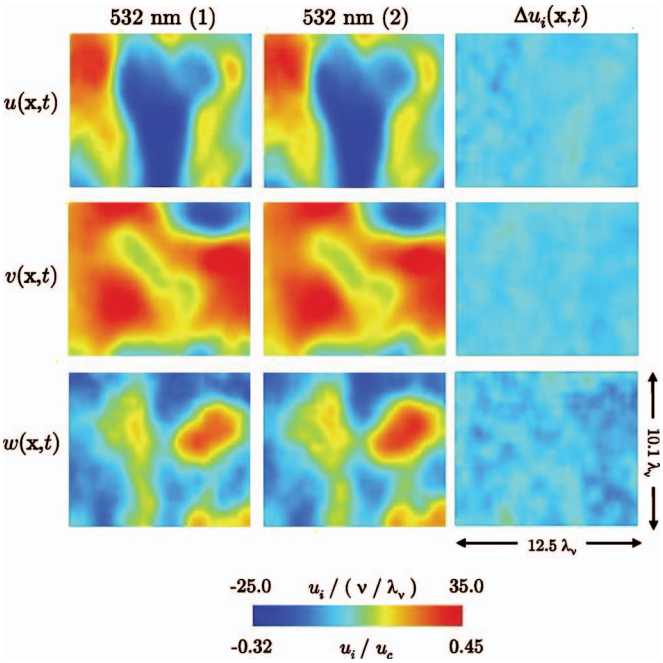

FIG. 6. (Color) Typical instantaneous velocity component fields $u_i(\mathbf{x},t)$ from single-plane DSPIV imaging assessments, showing independently measured fields from stereo camera pair 1 (left) and stereo camera pair 2 (middle). Also shown are corresponding difference fields $\Delta u_i(\mathbf{x},t)$ (right); note that measurement errors $\Delta u_i \ll u_i$.

logarithmic axes. The latter allows comparisons in the tails of the pdfs, corresponding to high-gradient features nearly 1000 times less common than the mean. In both figures there are two curves plotted in each panel, one from each independent stereo camera pair. As in Fig. 7, the differences between the two independent measurements in each panel are barely discernible, even at relatively large gradient values in Fig. 11. Moreover, the differences in relative widths between the on-diagonal $(i=j)$ and off-diagonal $(i \neq j)$ components of $\partial u_i / \partial x_j$ appear consistent with the requirements of isotropy. This is examined quantitatively in the following section.

V. COINCIDENT-PLANE DSPIV IMAGING ASSESSMENTS

An assessment that includes additional errors due to light sheet positioning inaccuracies and separate formation of green and red light sheet pairs can be obtained from coincident-plane DSPIV imaging tests. In this case, the velocity component fields obtained from the two independent stereo camera pairs are compared when the 532 and 635 nm light sheets are arranged to be as nearly coincident as possible. These assessments were made in the same flow under identical conditions as in Sec. IV, but with the two stereo camera pairs now imaging separate 532 and 635 nm light sheets positioned with the optical alignment system.

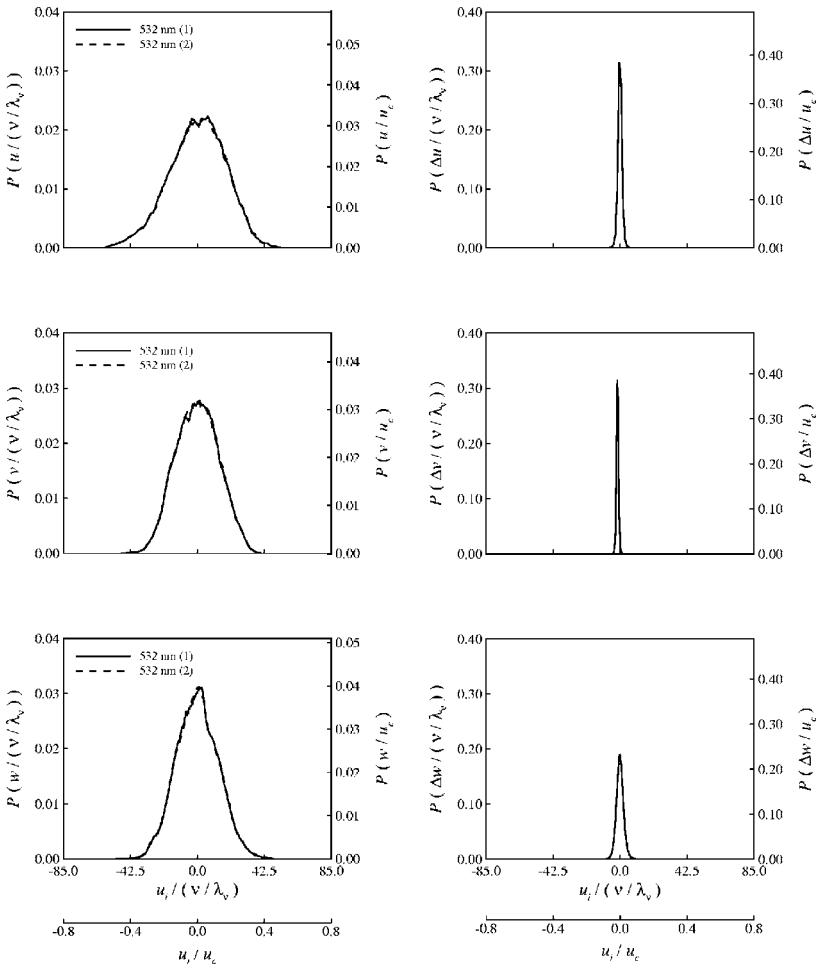

FIG. 7. Probability densities of measured velocity component fluctuation fields $u_i(\mathbf{x},t)$ from single-plane DSPIV imaging assessments (left); note there are two curves in each panel, one from each independent stereo camera pair. Also shown are pdfs of corresponding difference fields $\Delta u_i(\mathbf{x},t)$ (right), where it is apparent that the measurement errors $\Delta u_i \ll u_i$.

TABLE II. Rms errors in velocity component differences Δu_i from assessments based on single-plane imaging in Sec. IV and coincident-plane imaging in Sec. V.

		Single		Coincident	
Velocity component	$(u_i)_{\mathrm{rms}}$	$(\Delta u_i)_{\mathrm{rms}}$ (m/s)	$\frac{(\Delta u_i)_{\mathrm{rms}}}{(u_i)_{\mathrm{rms}}}$	$(\Delta u_i)_{\mathrm{rms}}$ (m/s)	$\frac{(\Delta u_i)_{\mathrm{rms}}}{(u_i)_{\mathrm{rms}}}$
u	0.24	0.011	4.6%	0.021	8.8%
v	0.20	0.013	6.5%	0.017	8.5%
w	0.21	0.022	10.5%	0.034	16.2%

A. Velocity differences

Figures 12 and 13 show typical examples of the instantaneous velocity vector fields $\mathbf{u}(\mathbf{x},t)$ measured independently in the coincident 532 and 635 nm light sheets. In principle, these velocity fields should be identical, with any differences resulting solely from the cumulative effects of the errors considered in Secs. III and IV and the additional errors introduced by the independent dual light sheet generation and positioning. Figure 13 shows the individual instantaneous velocity component fields $u_i(\mathbf{x},t)$ obtained independently from the 532 and 635 nm stereo camera pairs, with the differences $\Delta u_i(\mathbf{x},t)$ between the two sets of respective fields shown on the right in the same quantitative color scale. It is apparent that, as in Fig. 6 from the single-plane imaging assessments, the differences Δu_i between the two independent measurements in these coincident-plane imaging assessments are far smaller than the measured velocity component values themselves. This indicates that the additional errors

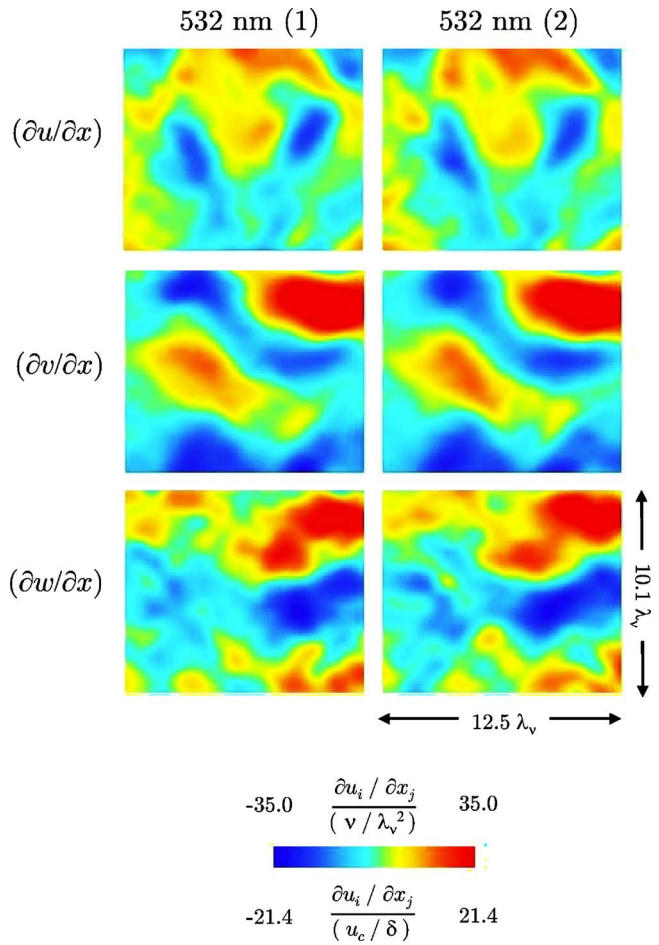

FIG. 8. (Color online) Typical instantaneous velocity gradient component fields $\partial u_i/\partial x$ from single-plane DSPIV imaging assessments, showing independently measured fields from camera pair 1 (left) and camera pair 2 (right). Results shown scaled on both local inner (λ_ν,ν) and outer (u_c,δ) variables.

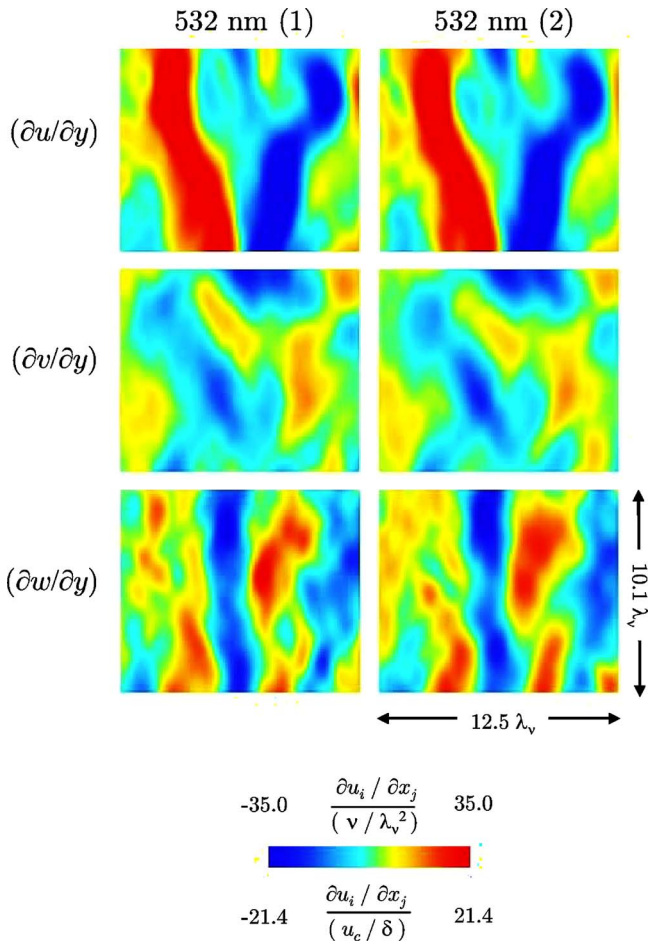

FIG. 9. (Color online) Typical instantaneous velocity gradient component fields $\partial u_i/\partial y$ from single-plane DSPIV imaging assessments, showing independently measured fields from camera pair 1 (left) and camera pair 2 (right). Results shown scaled on both local inner (λ_ν,ν) and outer (u_c,δ) variables.

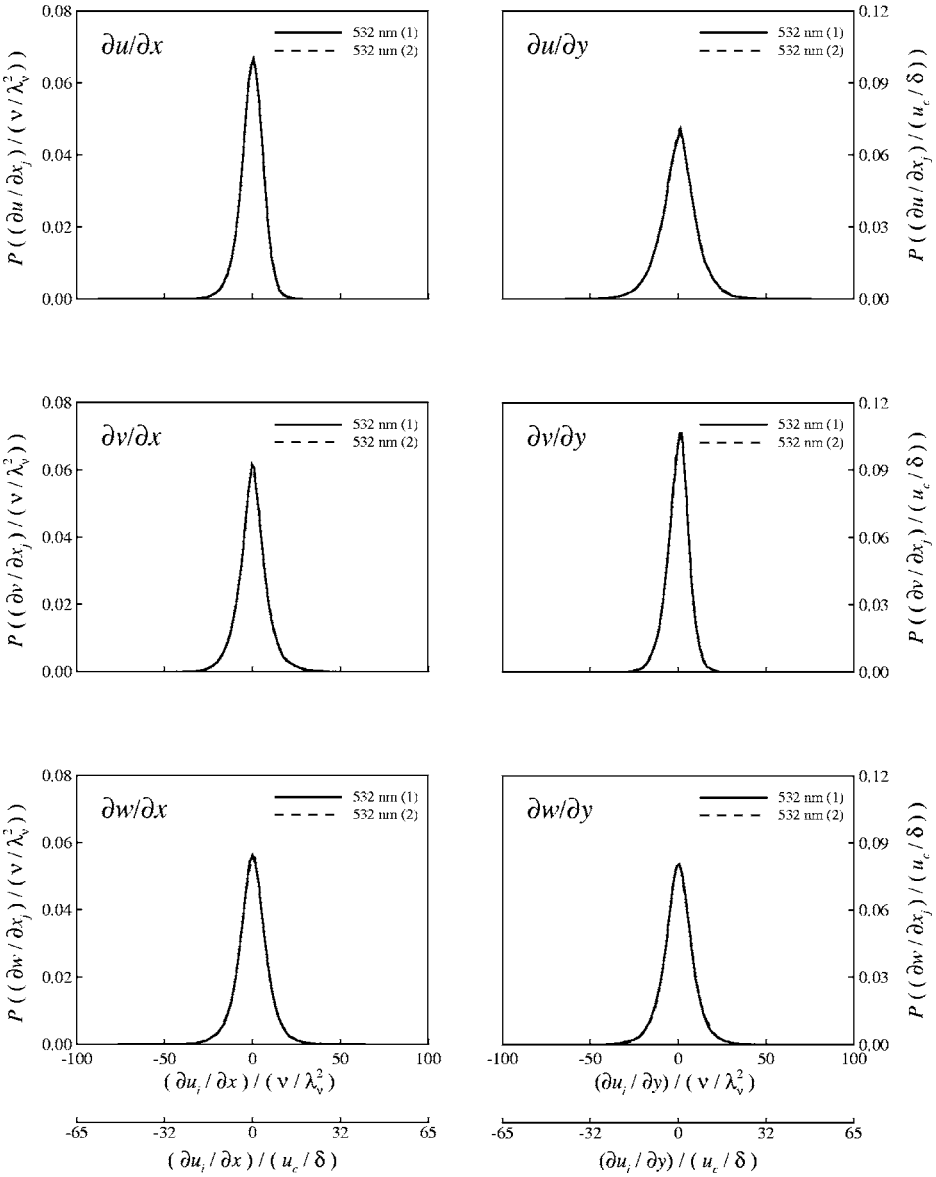

FIG. 10. Probability densities of measured velocity gradient components $\partial u_i/\partial x$ (left) and $\partial u_i/\partial y$ (right) from single-plane DSPIV imaging assessments. Note there are two curves in each panel, one for each independent stereo camera pair.

due to separate formation of the light sheet pairs and the associated light sheet positioning inaccuracies are substantially smaller than the errors inherent in the independent stereo imaging in Sec. IV.

Probability densities of the two sets of independently measured velocity components u_i and the corresponding differences Δu_i between the two measurements in these coincident-plane imaging assessments are shown, on the same scale, in Fig. 14. In each $P(u_i)$ panel there are two distributions shown, one from each of the independent stereo camera pairs. The distributions obtained from each camera pair are nearly identical. Moreover by comparing the Δu_i pdfs in Fig. 14 with those in Fig. 7 it is evident that the additional measurement errors due to the independent light sheet formation and positioning are relatively small. Table II gives the resulting rms values of these Δu_i distributions. These confirm that the largest errors arise in the w components, with the overall relative errors in the velocity differences found to be approximately 8%–9% for the in-plane components and 16% for the out-of-plane components.

B. Velocity gradients

Figures 15 and 16 show comparisons of the six measured velocity gradient component fields $\partial u_i/\partial x$ and $\partial u_i/\partial y$ accessible by such coincident-plane imaging assessments, obtained independently from the two stereo camera pairs. As was the case for the corresponding single-plane assessments in Figs. 8 and 9, the resulting velocity gradients are largely the same from both camera pairs, providing further verification of the accuracy of velocity gradient fields from DSPIV measurements.

Probability densities for each of these six velocity gradient components are shown in Fig. 17 in linear axes and in Fig. 18 in semilogarithmic axes. In both figures there are two curves plotted in each panel, one obtained from each independent stereo camera pair. As in Figs. 10 and 11, the differences between the two independently measured curves in each panel are barely discernible, both in the linear and the semilogarithmic forms.

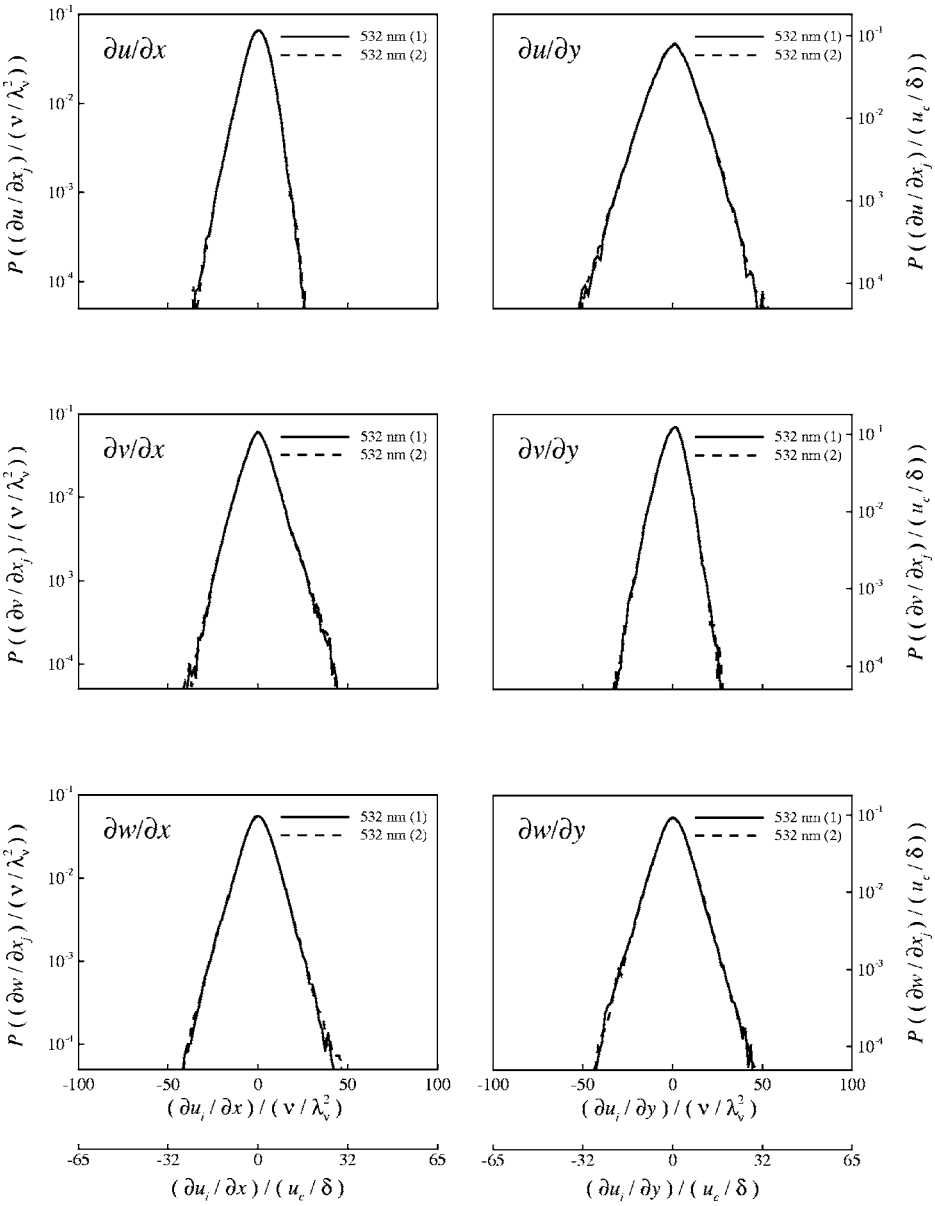

FIG. 11. Same as Fig. 10 but showing probability densities of measured velocity gradient components from single-plane DSPIV imaging assessments in semilogarithmic axes to allow comparisons in pdf tails. Note there are two independently measured curves in each panel.

C. Isotropy tests

Further quantification of the accuracy of velocity gradient component fields from such coincident-plane imaging tests can be obtained by comparing various combinations of measured velocity gradient moments with corresponding values for homogeneous isotropic turbulence. The velocity gradients $\partial u_i/\partial x_j$ inherently result from differences in the velocity component values at closely spaced points, with the consequence that contributions from the large scales cancel almost entirely. Statistics of the measured velocity gradient components are thus determined primarily by the intermediate and small scales of the flow. The classical assumption of local isotropy at sufficiently small scales suggests that these scales should approach a locally homogeneous and isotropic state, and thus comparisons with isotropic values are meaningful for the velocity gradients statistics. While small departures from perfect isotropy in the velocity gradients at these scales may expected due to weak residual contributions from the large scales at these Reynolds numbers, measured velocity gradient statistics would be expected to at least approach corresponding isotropic values.

Central to such assessments are the results from incompressible homogeneous isotropic turbulence that mean-square values of longitudinal and transverse derivatives of the velocity components must follow

$$\left[\overline{\left(\frac{\partial u_i}{\partial x_j}\right)^2}\right]_{i=j} = \frac{1}{15}\left(\frac{\varepsilon}{\nu}\right), \tag{1}$$

$$\left[\overline{\left(\frac{\partial u_i}{\partial x_j}\right)^2}\right]_{i\neq j} = \frac{2}{15}\left(\frac{\varepsilon}{\nu}\right), \tag{2}$$

where ε and ν are the mean kinetic energy dissipation rate and the viscosity. To test the similarity implied by (1) and (2) in the on-diagonal and off-diagonal components of the measured velocity gradients, Fig. 19 shows each of the six com-

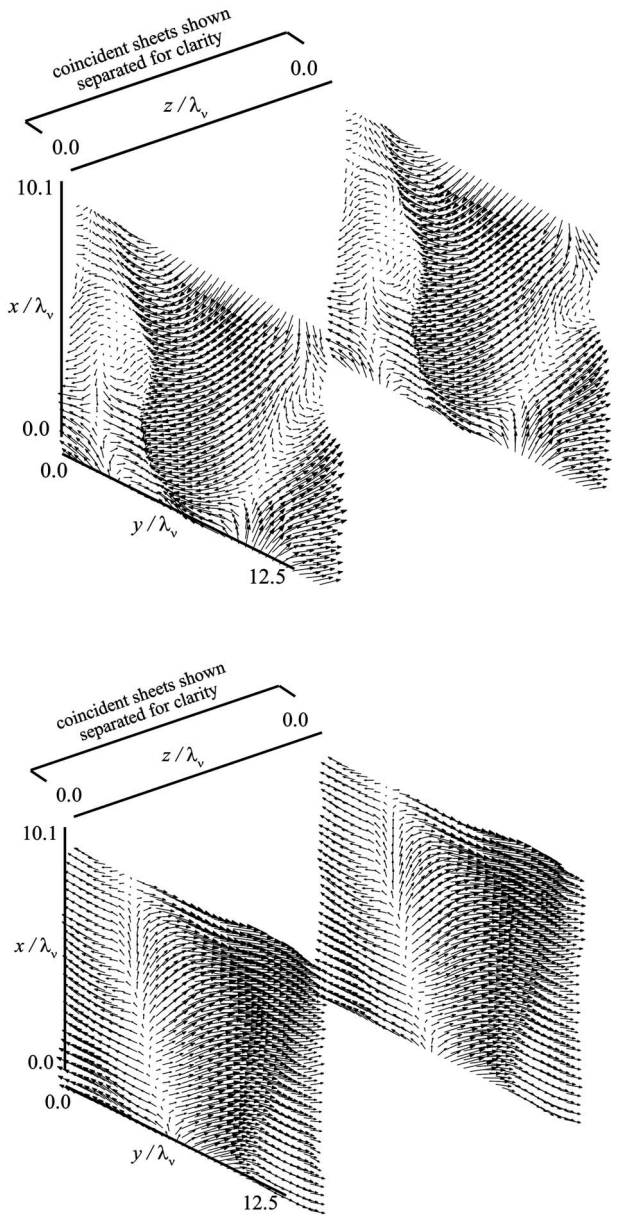

FIG. 12. Two typical instantaneous velocity vector fields $\mathbf{u}(\mathbf{x},t)$ from coincident-plane DSPIV imaging assessments, showing independently measured fields from both stereo camera pairs. To allow clearer comparisons, mean velocity has been subtracted and coincident planes are shown separated.

ponent pdfs from Fig. 18 on the same axes. It is apparent that the two on-diagonal ($i=j$) and four off-diagonal ($i\neq j$) components very nearly satisfy the similarity requirements. Moreover, consistent with the isotropy requirements in (1) and (2), the pdfs in Fig. 19 suggest a significantly larger mean-square value in the off-diagonal components than in the on-diagonal components, as evidenced by the greater widths of these pdfs. This can be quantified by various combinations of the measured mean-square velocity gradient component values for comparison with the corresponding isotropic values from (1) and (2).

These coincident-plane imaging tests provide access to six of the nine velocity gradient components, namely the x and y derivatives of the u, v, and w velocity components.

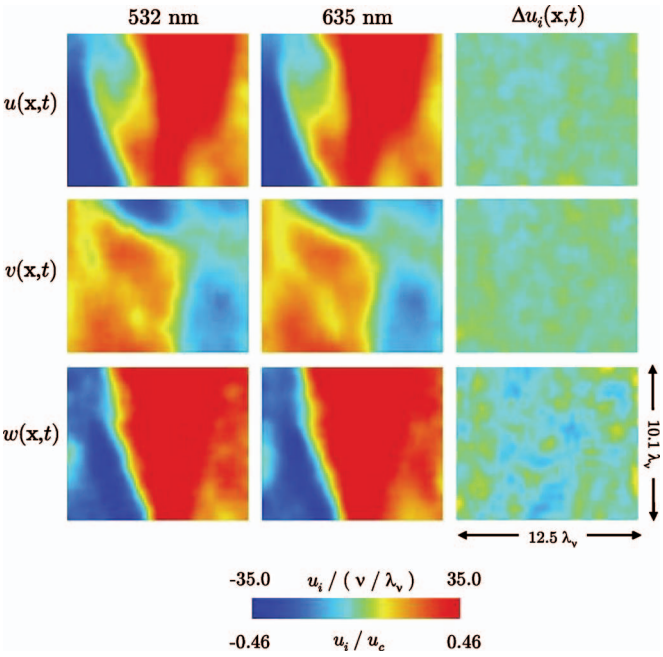

FIG. 13. (Color) Typical instantaneous velocity component fields $u_i(\mathbf{x},t)$ from coincident-plane DSPIV imaging assessments, showing independently measured fields from 532 nm camera pair (left) and from 635 nm camera pair (middle). Also shown are corresponding difference fields $\Delta u_i(\mathbf{x},t)$ (right) where it is apparent that DSPIV measurement errors $\Delta u_i \ll u_i$.

Among these, three combinations are of particular interest, since they allow separate assessments of the accuracies of the in-plane and out-of-plane velocity gradient components. In particular, an assessment of only the w-derivative components is obtained from the measured ratio

$$\frac{\overline{\left(\frac{\partial w}{\partial y}\right)^2}}{\overline{\left(\frac{\partial w}{\partial x}\right)^2}} \approx 1.09, \tag{3}$$

which may be compared with the corresponding ideal isotropic value of 1 from (2), suggesting that the w-derivative components are reasonably accurate. An assessment involving only the u- and v-derivative components is also possible via the measured ratio

$$\frac{\overline{\left(\frac{\partial u}{\partial y}\right)^2}+\overline{\left(\frac{\partial v}{\partial x}\right)^2}}{\overline{\left(\frac{\partial u}{\partial x}\right)^2}+\overline{\left(\frac{\partial v}{\partial y}\right)^2}} \approx 1.99, \tag{4}$$

which should be compared with the corresponding isotropic limit value of 2 from (1) and (2). This further suggests that these derivative components are also reasonably accurate. A further assessment involving all six of the gradient components available from such coincident-plane DSPIV imaging tests, which compares derivatives of the out-of-plane to in-plane velocity components, is possible via the measured ratio

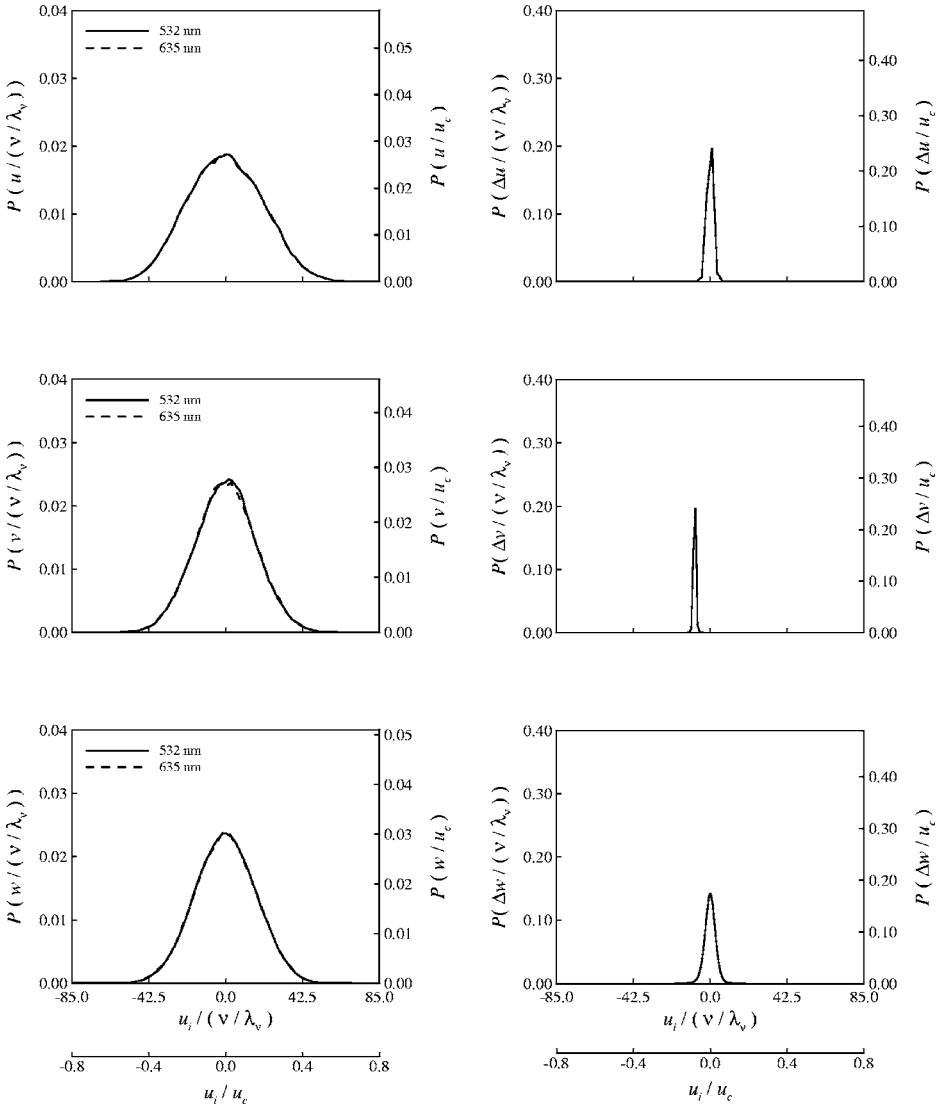

FIG. 14. Probability densities of measured velocity gradient components $\partial u_i/\partial x$ (left) and $\partial u_i/\partial y$ (right) from coincident-plane DSPIV imaging assessments; note there are two curves in each panel, one from each independent stereo camera pair.

$$\frac{\overline{\left(\frac{\partial w}{\partial x}\right)^2}+\overline{\left(\frac{\partial w}{\partial y}\right)^2}}{\overline{\left(\frac{\partial u}{\partial x}\right)^2}+\overline{\left(\frac{\partial u}{\partial y}\right)^2}+\overline{\left(\frac{\partial v}{\partial x}\right)^2}+\overline{\left(\frac{\partial v}{\partial y}\right)^2}}\approx 0.64. \tag{5}$$

From (1) and (2), this may be compared to the corresponding ideal isotropic limit value of 2/3, and further indicates that errors in the measured velocity gradient components from such coincident-plane imaging assessments are typically of the order of a few percent.

VI. SEPARATED-PLANE DSPIV IMAGING ASSESSMENTS

Assessments of the accuracy of DSPIV velocity gradient measurements that take into account all nine simultaneously measured components of $\partial u_i/\partial x_j$ are possible from separated-plane imaging tests. These assessments were made in the same turbulent shear flow under identical conditions as in Secs. IV and V, but with the two stereo camera pairs now imaging individual 532 and 635 nm light sheet pairs arranged with a differential separation $\Delta z \approx 400\ \mu$m that matches the in-plane separation between adjacent vectors.

A. Typical DSPIV measurement results

Figure 20 shows a typical example of the instantaneous measured velocity vector fields $\mathbf{u}(\mathbf{x},t)$ in the two differentially spaced planes. As before, the respective mean velocity for each component has been subtracted to better show the fluctuations, and the separation in the z direction is greatly exaggerated to better show the vectors in both planes. In these separated-plane tests, the velocity fields in the two planes should no longer be identical. The relatively small differences in the vectors between each pair of planes are due to the differential z spacing. It is these differences that give rise to the z-derivative components of the resulting velocity gradient tensor fields $\partial u_i/\partial x_j$.

Figure 21 gives a typical example of all three simultaneously measured instantaneous velocity component fields $u_i(\mathbf{x},t)$ in the two differentially spaced 532 and 635 nm light sheet planes. The dimensions of each plane are indicated in terms of the local inner (viscous) length scale λ_ν of the tur-

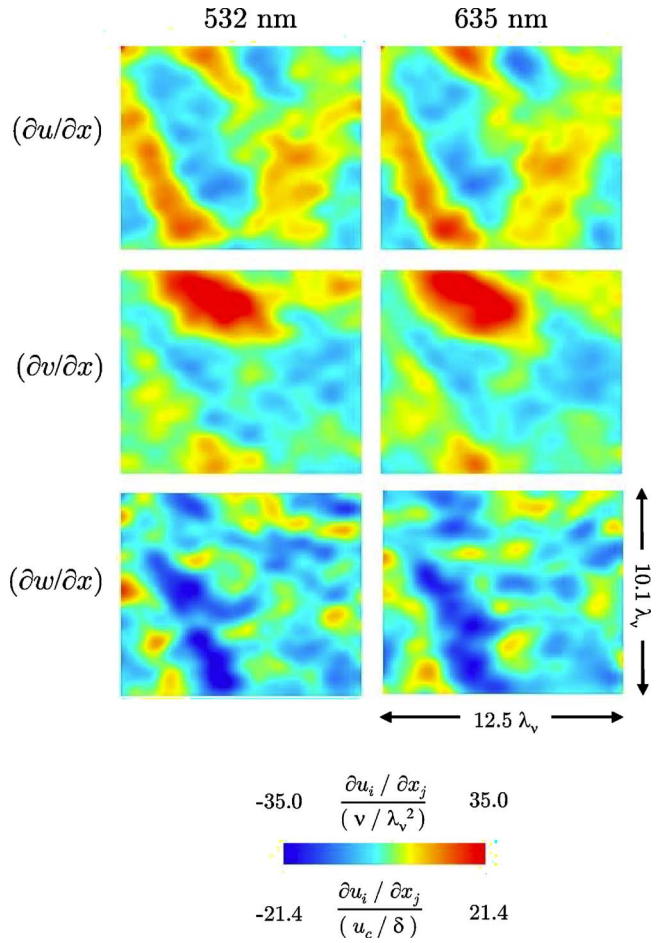

FIG. 15. (Color online) Typical instantaneous velocity gradient component fields $\partial u_i/\partial x$ from coincident-plane DSPIV imaging assessments, showing independently measured derivative fields from 532 nm (left) and 635 nm (right) stereo camera pairs. Results shown scaled on both local inner (λ_ν, ν) and outer (u_c, δ) variables.

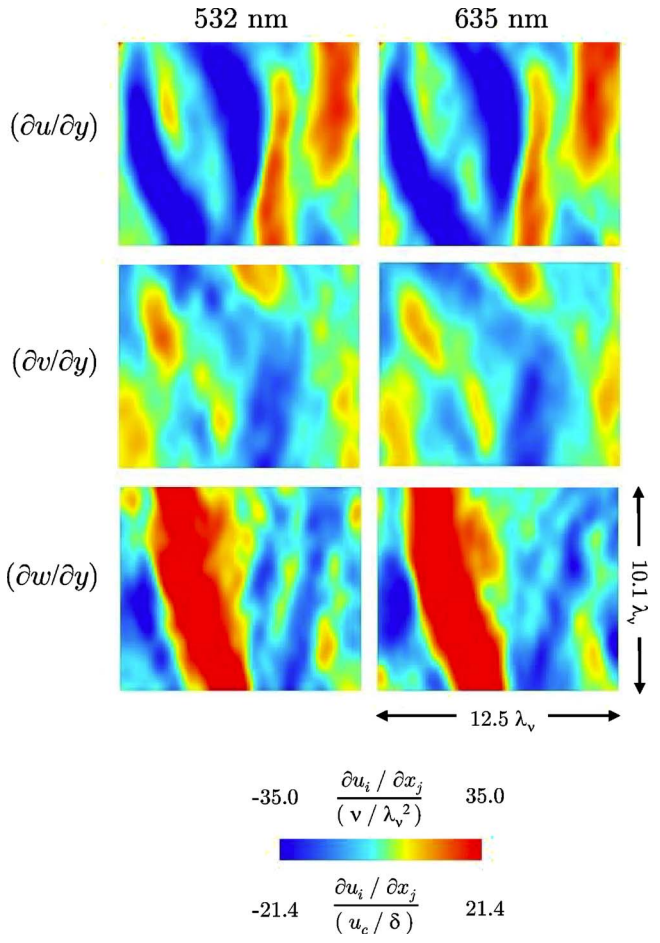

FIG. 16. (Color online) Typical instantaneous velocity gradient component fields $\partial u_i/\partial y$ from coincident-plane DSPIV imaging assessments, showing independently measured derivative fields from 532 nm (left) and 635 nm (right) stereo camera pairs. Results shown scaled on both local inner (λ_ν, ν) and outer (u_c, δ) variables.

bulent shear flow.[35,36] The color scale gives the velocity component values normalized by the local outer velocity scale u_c as well as by the local inner velocity scale (ν/λ_ν). The small differences discernible between the $u_i(\mathbf{x},t)$ fields in the 532 nm and 635 nm planes due to the differential z spacing produce the z-derivative components of the velocity gradient tensor fields $\partial u_i/\partial x_j$.

Figure 22 shows a typical example of all nine simultaneously measured components of the instantaneous velocity gradient tensor field $\partial u_i/\partial x_j$. The velocity gradient fields were obtained by central differences of the measured velocity component values within each plane and one-sided differencing between the two planes. The differencing template used the natural pixel-based coordinate frame as well as the two additional frames resulting from 45° rotations around the x and z axes. This makes use of all 18 points in the $3\times3\times2$ template around each point to provide reduction of random error without degrading the spatial resolution in the resulting derivative fields. The dimensions of major structural features in each of these velocity gradient component planes are consistent with the local inner length scale λ_ν of the flow.

Probability densities of the three on-diagonal $(i=j)$ and six off-diagonal $(i\neq j)$ components of the velocity gradients are presented, respectively, in linear and semilogarithmic forms, in Figs. 23 and 24. These are formed from over 1200 individual data planes of the type in Fig. 22, each containing all nine gradient tensor components at 736 independent points on the 32×23 grid shown in Fig. 20. These pdfs suggest both the similarity among components and the differing relative widths between on- and off-diagonal components demanded by incompressibility and isotropy in (1) and (2). Such isotropy tests, presented below, provide a further means to assess the accuracy of velocity gradient measurements with DSPIV.

B. Gradient assessments based on isotropy tests

Ideal isotropy would require the pdfs for the three on-diagonal components of the velocity gradients $\partial u_i/\partial x_j$ to be identical, and the pdfs for the six off-diagonal components to also be identical. In Figs. 23 and 24 there is strong evidence for such isotropy, as seen by the similarity of the pdfs for each of the velocity gradient components in each panel. The semilogarithmic forms, in the lower panel of each figure, verify that this similarity holds even for rare large-gradient

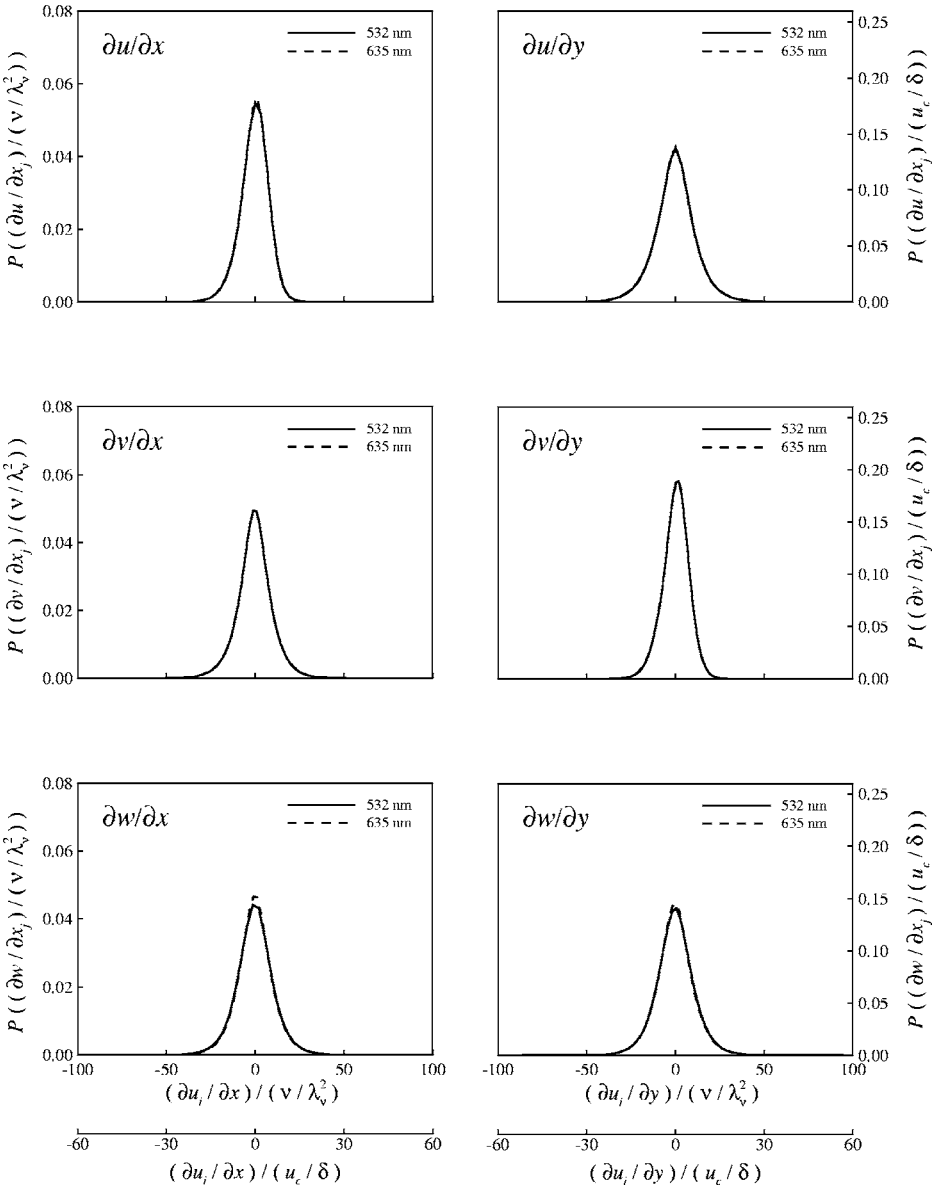

FIG. 17. Probability densities of measured velocity gradient components $\partial u_i/\partial x$ (left) and $\partial u_i/\partial y$ (right) from coincident-plane DSPIV imaging assessments; note there are two curves in each panel, one from each independent stereo camera pair.

features represented by the tails of these pdfs, which have a frequency of occurrence nearly 10^4 times lower than the mean.

Additionally, the ideal isotropy requirements in (1) and (2) imply a $\sqrt{2}$ difference in the relative widths of the pdfs for the on- and off-diagonal components of the velocity gradient pdfs. Comparing the lower panels in Figs. 23 and 24 suggests such a difference in widths. The average value of the second moments, normalized on inner variables, for the on-diagonal components is 6.93 and for the off-diagonal components is 9.64. The resulting ratio is 1.39, and is within 1.6% of the $\sqrt{2}$ factor from (1) and (2).

The second moments of the measured velocity gradient components allow further assessments of the accuracy of these DSPIV measurements by comparing ratios of combinations of mean-square gradient components with the corresponding incompressible isotropic values from (1) and (2). There are three such combinations that are of particular interest, since they allow various aspects of the velocity gradients to be isolated. The first is based on the ratio of on-diagonal to off-diagonal gradient components, with the measured value being

$$\frac{\overline{\left(\frac{\partial u}{\partial x}\right)^2}+\overline{\left(\frac{\partial v}{\partial y}\right)^2}+\overline{\left(\frac{\partial w}{\partial z}\right)^2}}{\overline{\left(\frac{\partial u}{\partial y}\right)^2}+\overline{\left(\frac{\partial u}{\partial z}\right)^2}+\overline{\left(\frac{\partial v}{\partial x}\right)^2}+\overline{\left(\frac{\partial v}{\partial z}\right)^2}+\overline{\left(\frac{\partial w}{\partial x}\right)^2}+\overline{\left(\frac{\partial w}{\partial y}\right)^2}} \approx 0.26. \tag{6}$$

From (1) and (2), this compares well with the ideal isotropic value of 1/4. A second combination examines the ratio of w-gradient components to u- and v-gradient components, for which the measured value is

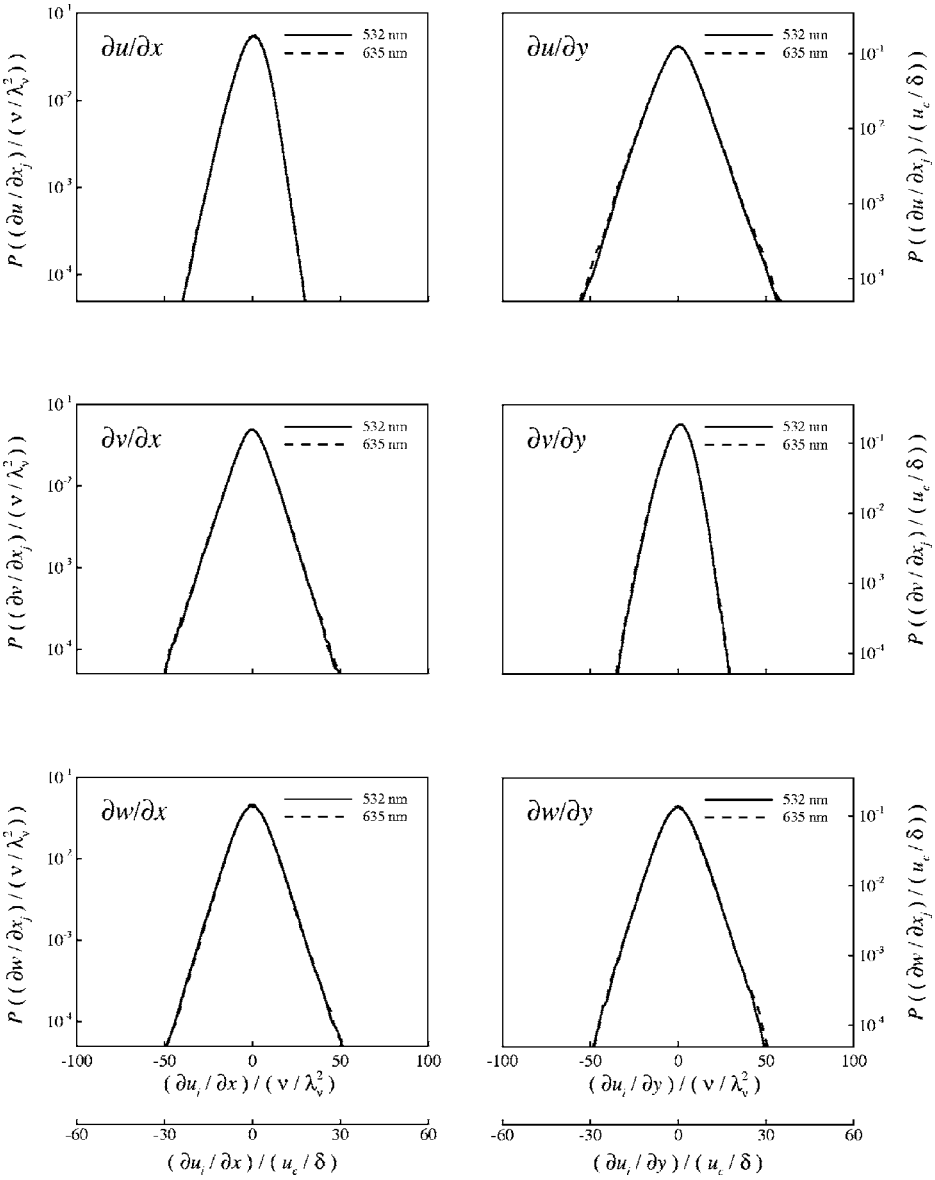

FIG. 18. Same as Fig. 17 but showing probability densities of measured velocity gradient components from coincident-plane DSPIV imaging assessments in semilogarithmic axes to allow comparisons of rare-event tails. Note there are two independently measured curves in each panel.

$$\frac{\overline{\left(\frac{\partial w}{\partial x}\right)^2}+\overline{\left(\frac{\partial w}{\partial y}\right)^2}+\overline{\left(\frac{\partial w}{\partial z}\right)^2}}{\overline{\left(\frac{\partial u}{\partial x}\right)^2}+\overline{\left(\frac{\partial u}{\partial y}\right)^2}+\overline{\left(\frac{\partial u}{\partial z}\right)^2}+\overline{\left(\frac{\partial v}{\partial x}\right)^2}+\overline{\left(\frac{\partial v}{\partial y}\right)^2}+\overline{\left(\frac{\partial v}{\partial z}\right)^2}} \approx 0.51. \quad (7)$$

From (1) and (2), this may be compared with the ideal isotropic value of 1/2. A final combination examines the ratio of z-derivative components to x- and y-derivative components, for which the resulting measured value is

$$\frac{\overline{\left(\frac{\partial u}{\partial z}\right)^2}+\overline{\left(\frac{\partial v}{\partial z}\right)^2}+\overline{\left(\frac{\partial w}{\partial z}\right)^2}}{\overline{\left(\frac{\partial u}{\partial x}\right)^2}+\overline{\left(\frac{\partial u}{\partial y}\right)^2}+\overline{\left(\frac{\partial v}{\partial x}\right)^2}+\overline{\left(\frac{\partial v}{\partial y}\right)^2}+\overline{\left(\frac{\partial w}{\partial x}\right)^2}+\overline{\left(\frac{\partial w}{\partial y}\right)^2}} \approx 0.50. \quad (8)$$

For this combination, the corresponding ideal isotropic value is 1/2. Collectively, these moment combinations provide further quantitative support for the validity of the measured velocity gradient components obtained from the present DSPIV system in turbulent shear flows.

C. Measured divergence errors

A further stringent test of the accuracy of velocity gradient measurements can be based on the measured divergence errors, which determines the extent to which the resulting data satisfy the zero divergence condition $\nabla \cdot \mathbf{u} \equiv 0$ demanded by incompressibility. Few studies have reported such measured divergence values, yet this provides one of the most fundamental tests for the accuracy of the resulting velocity derivatives. Reference 10 gives divergence errors from holographic PIV measurements of velocity gradients in a turbulent flow. As expected, in their results computation of the divergence over increasingly larger volumes led to reduced error values (see their Figs. 9 and 10); at the full measurement resolution $W \approx 930$ μm, the reported mean di-

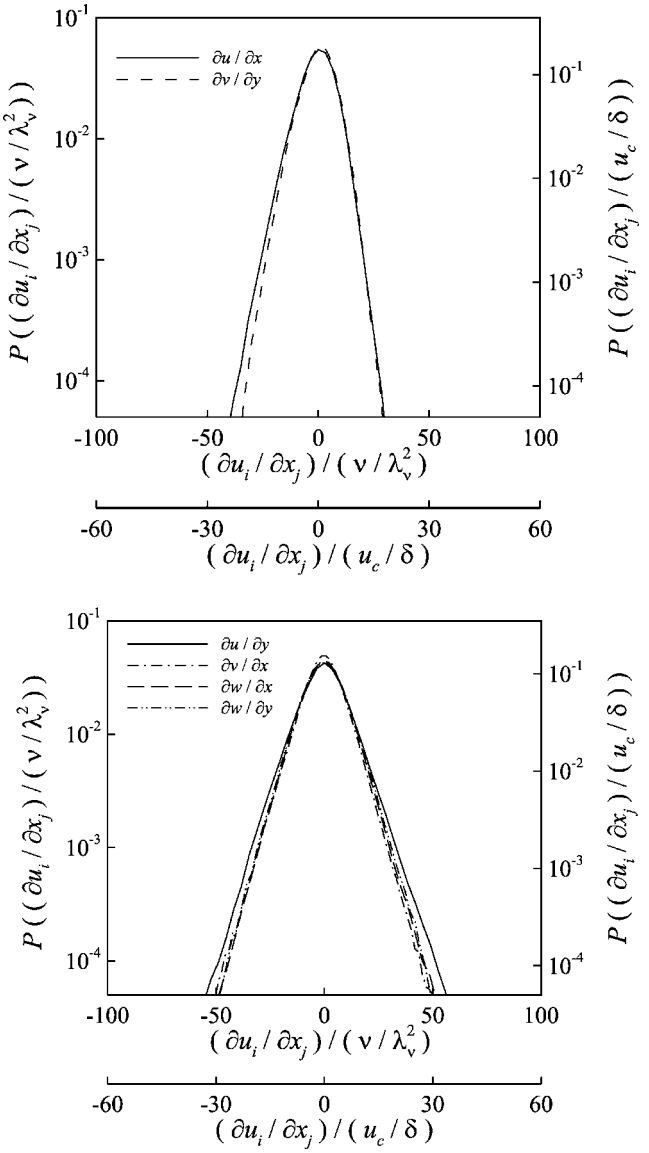

FIG. 19. Probability densities of measured velocity gradient components from coincident-plane DSPIV imaging assessments, showing similarity suggested by isotropy in on-diagonal (top) and off-diagonal (bottom) components of velocity gradients $\partial u_i/\partial x_j$, as well as differences in relative widths.

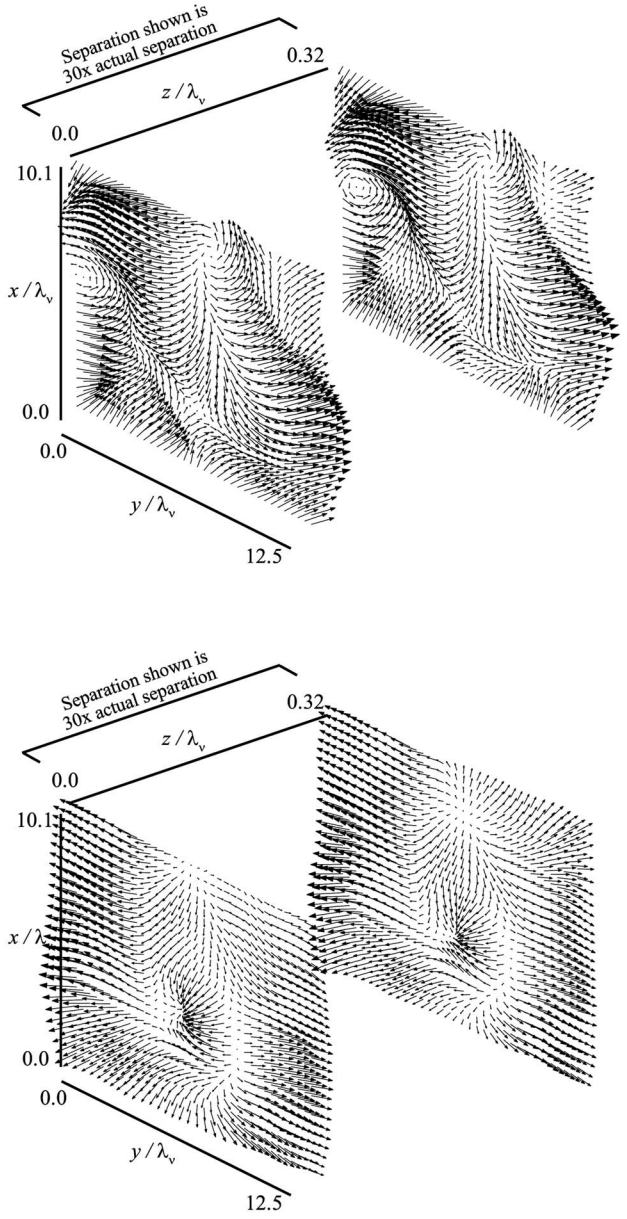

FIG. 20. Two typical instantaneous velocity vector fields $\mathbf{u}(\mathbf{x},t)$ from separated-plane DSPIV imaging assessments showing measured velocity fields in two planes with 400 μm z separation. Interplane separation shown greatly exaggerated; actual separation between planes is same as vector-to-vector spacing within each plane. Axes shown normalized by local inner length scale λ_ν.

vergence error $(\partial u_i/\partial x_i)^2$ was 74% of the local $(\partial u/\partial x)^2+(\partial v/\partial y)^2+(\partial w/\partial z)^2$ value. Figure 25 gives the probability density of the measured divergence values for the present DSIV measurements. Here the local divergence values $\nabla\cdot\mathbf{u}$ have been normalized by the local norm $(\nabla\mathbf{u}:\nabla\mathbf{u})^{1/2}$ of the velocity gradient tensor to give an indication of the relative magnitude of the local divergence errors. The resulting rms value is 0.35, which is roughly consistent with the rms errors of 9% and 16% in each of the in-plane and out-of-plane velocity differences obtained from the coincident-plane imaging tests.

VII. CONCLUSIONS

The present results have demonstrated the accuracy of dual-plane stereo particle imaging velocimetry (DSPIV) to allow direct nontrusive highly resolved measurements all nine simultaneous components of the velocity gradient tensor fields $\partial u_i/\partial x_j$ at intermediate and small scales of turbulent shear flows. These results have also provided strict quantitative assessments of the accuracy of the velocity gradients obtained from such DSPIV measurements, and have indicated the origins of the principal remaining errors in such measurements.

In particular, intrinsic error limits introduced by the asymmetric stereo PIV imaging arrangement have been quantified here in assessments based on synthetic particle imaging, with errors in velocity differences found in Table I to be at most 0.8%. Additional errors introduced by limits on the accuracy of true particle imaging in a finite-thickness light sheet have here been rigorously quantified through

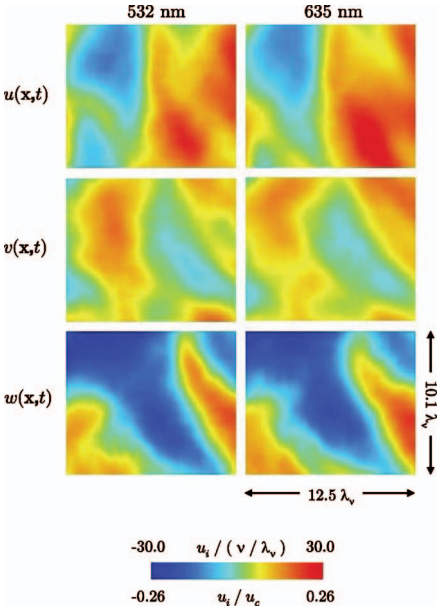

FIG. 21. (Color) Typical instantaneous velocity component fields $u_i(\mathbf{x},t)$, from separated-plane DSPIV imaging assessments, showing measured velocity fields in 532 nm (left) and 635 nm (right) planes separated by $\Delta z/\lambda_\nu=0.32$. Field of view shown normalized by local inner length scale λ_ν. Color scale shows quantitative values normalized on local inner (ν,λ_ν) and outer (u_c,δ) scales.

single-plane DSPIV imaging assessments in a turbulent shear flow. These errors have been shown to be significantly larger than the intrinsic error limits, with the largest errors in the measured out-of-plane velocity component. These errors

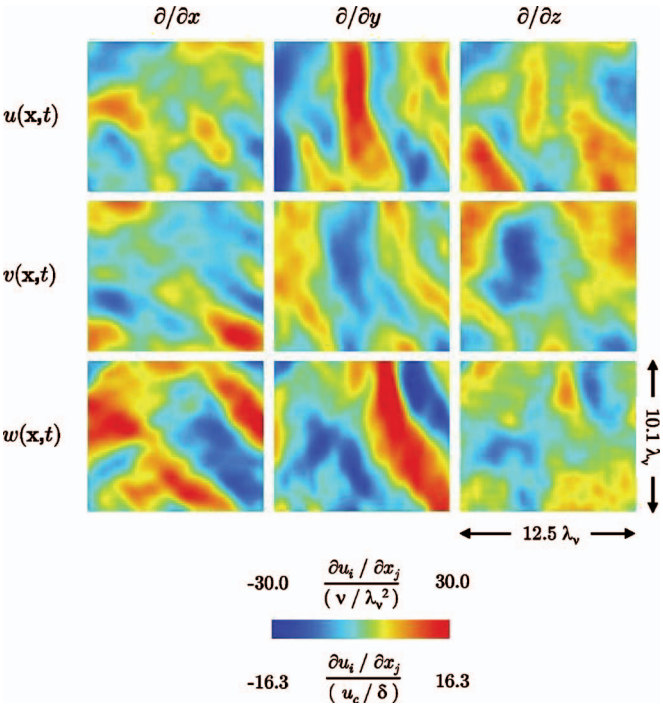

FIG. 22. (Color) Typical full nine-component velocity gradient tensor fields $\partial u_i/\partial x_j(\mathbf{x},t)$ from separated-plane DSPIV imaging assessments. Field of view shown normalized by local inner length scale λ_ν. Color scale shows quantitative values normalized both on local inner (ν,λ_ν) and outer (u_c,δ) scales.

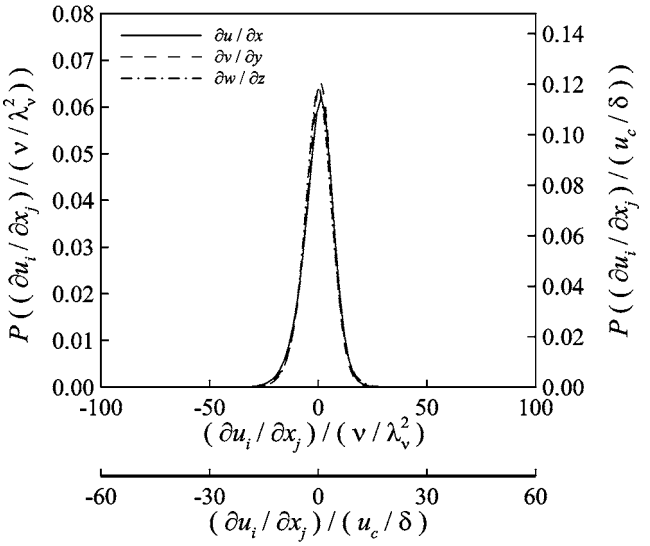

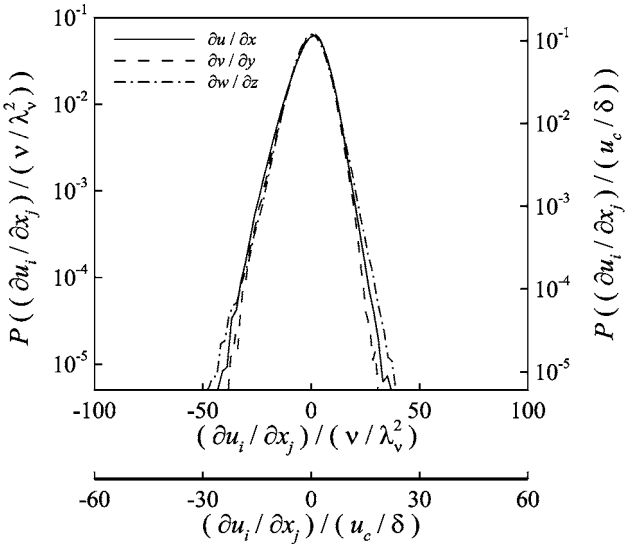

FIG. 23. Probability densities of on-diagonal components of $\partial u_i/\partial x_j$ from separated-plane DSPIV imaging assessments, shown scaled on local inner (ν,λ_ν) and outer (u_c,δ) variables in linear (top) and semilogarithmic (bottom) forms. Resulting similarity indicates near isotropy in velocity gradient fields at these scales.

were shown in Table II to be of the order 6% in the in-plane components and 10% in the out-of-plane components. Further errors introduced by limits in the accuracy of independent dual light sheet generation and positioning have been rigorously quantified through coincident-plane DSPIV imaging assessments in the same turbulent shear flow. These coincident-plane assessments show resulting errors in velocity differences in Table II to be of the order of 9% and 16% in the in-plane and out-of-plane components. Probability densities of the measured velocity gradient components show good agreement with the similarity and relative widths suggested by isotropy, and yield ratios of mean-square gradient values within a few percent of corresponding isotropic values.

Further assessments of the accuracy in practical velocity gradient measurements with this approach in turbulent shear

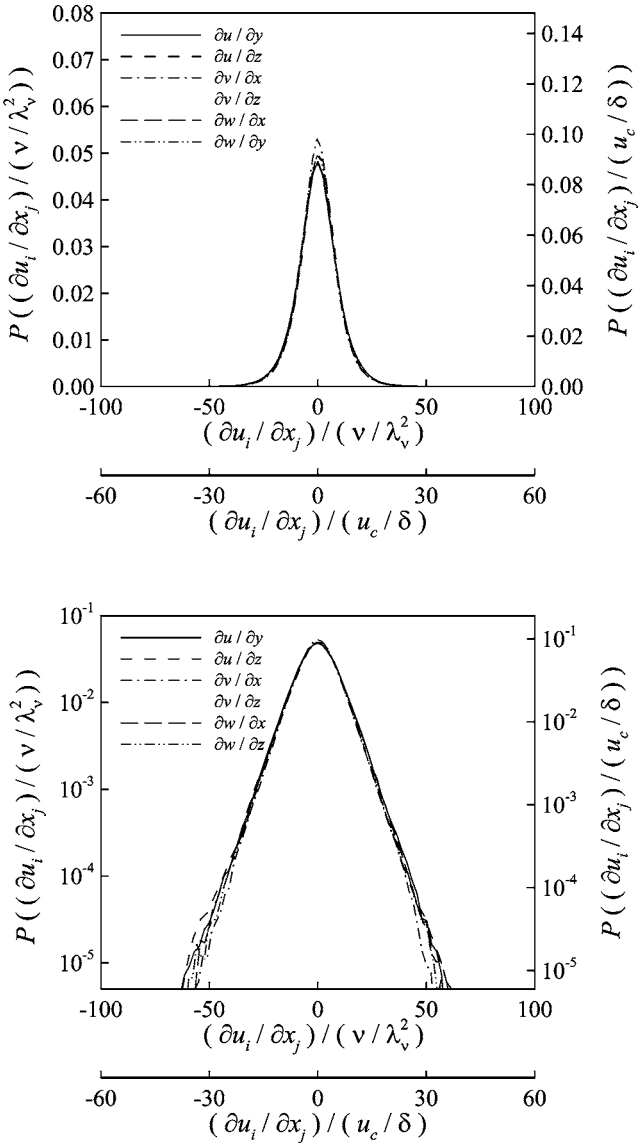

FIG. 24. Probability densities of off-diagonal components of $\partial u_i/\partial x_j$ from separated-plane DSPIV imaging assessments, shown scaled on local inner (ν,λ_ν) and outer (u_c,δ) variables in linear (top) and semilogarithmic (bottom) forms. Resulting similarity and widths relative to Fig. 23 indicate near-isotropy in velocity gradient fields at these scales.

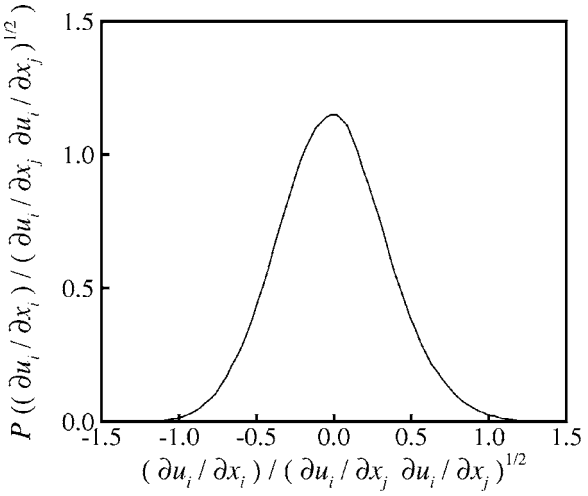

FIG. 25. Measured divergence errors $\nabla\cdot\mathbf{u}$ from separated-plane DSPIV imaging assessments, showing probability density for local ratio of divergence and velocity gradient norm $(\nabla\mathbf{u}:\nabla\mathbf{u})^{1/2}$.

flows have been here obtained from separated-plane DSPIV imaging assessments at the intermediate and small scales of a turbulent shear flow. The resulting measured velocity gradient components show excellent similarity in the on-diagonal $(i=j)$ and off-diagonal $(i\neq j)$ components of $\partial u_i/\partial x_j$. Moreover, ratios of mean-square values from the measured gradient components show agreement within 4% of the requirements from isotropy. The present results have also provided experimental values for the measured velocity divergence errors $\nabla\cdot\mathbf{u}$ as a rigorous means of quantifying the accuracy of velocity gradient fields obtained from such DSPIV measurements. These results show that the measured $\nabla\cdot\mathbf{u}$ errors are significantly smaller than the individual measured velocity gradient components.

Collectively, such DSPIV measurements have here been shown to be capable of providing direct experimental access to all nine simultaneous velocity gradient component fields at the intermediate and small scales of fully developed turbulent shear flows under conditions that are, at present, beyond the reach of direct numerical simulation (DNS). Proper design of such DSPIV measurements thus allows direct highly resolved experimental studies of these quasi-universal intermediate and small scales in key gradient fields, such as the vorticity vector field, the strain rate tensor field, and the true kinetic energy dissipation rate field, in turbulent shear flows. Reference 23 presents such highly resolved measurements at outer-scale Reynolds numbers up to 30,000 to examine the structure, statistics, similarity and scaling of velocity gradient fields in turbulent shear flows. That study gives results for measured gradient fields at two different values of the outer-scale Reynolds number Re_δ and at two different mean shear values S in the flow to determine the extent to which classical turbulence theory accounts for the effects of Reynolds number and mean shear on the underlying turbulence structure and dynamics in turbulent shear flows. Moreover, since the present method is based on the use of two different light-sheet frequencies in conjunction with filters to separate the scattered light onto the individual stereo camera pairs, this allows traditional solid metal oxide particles to be used as the seed, thereby in principle permitting comparable DSPIV measurements in exothermic reacting flows. Such comparisons provide a means for experimentally obtaining insights into the effects of heat release on the structure, statistics, similarity and scaling of the intermediate and small scales of turbulent shear flows.

ACKNOWLEDGMENTS

This work was jointly supported, in part, by the National Aeronautics and Space Administration (NASA) Marshall and Glenn Research Centers and the Department of Defense (DoD) within the NASA Constellation University Institutes Project (CUIP) Space Vehicle Technology Institute (SVTI) under Grant No. NCC3-989, with Claudia Meyer as the project manager. Discussions with Professor Nao Ninomiya

are gratefully acknowledged, as is the assistance of Zac Nagel in conducting the measurements and Dr. Uwe Dierksheide and Dr. Callum Gray of LaVision, GmbH with the DSPIV acquisition software development. Dr. Cam Carter and Dr. Jeff Donbar of AFRL kindly provided the dye lasers.

[1] C. Meneveau and J. Katz, "Scale-invariance and turbulence models for large-eddy simulation," Annu. Rev. Fluid Mech. **32**, 1 (2000).
[2] G. K. Batchelor and A. A. Townsend, "The nature of turbulent motion at large wave-numbers," Proc. R. Soc. London, Ser. A **199**, 238 (1949).
[3] L. S. G. Kovasznay, "Turbulence measurements," in *High Speed Aerodynamics and Jet Propulsion*, edited by R. W. Landenbuerg, B. Lewis, R. N. Pease, and H. S. Taylor (Princeton University Press, Princeton, 1954), pp. 213–285.
[4] J. F. Foss, "Accuracy and uncertainty of transverse vorticity measurements," Bull. Am. Phys. Soc. **21**, 1237 (1976).
[5] J. Balint, J. M. Wallace, and P. Vukoslavcevic, "The velocity and vorticity fields of a turbulent flow. Part 1. Simultaneous measurements by hot-wire anemometry," J. Fluid Mech. **228**, 25 (1991).
[6] J. M. Wallace and J. F. Foss, "The measurements of vorticity in turbulent flows," Annu. Rev. Fluid Mech. **27**, 469 (1995).
[7] R. A. Antonia, T. Zhou, and Y. Zhu, "Three-component vorticity measurements in a turbulent grid flow," J. Fluid Mech. **374**, 29 (1998).
[8] A. Tsinober, E. Kit, and T. Dracos, "Experimental investigation of the field of velocity gradients in turbulent flows," J. Fluid Mech. **242**, 169 (1992).
[9] E. Kit, A. Tsinober, and T. Dracos, "Velocity-gradients in a turbulent jet flow," Appl. Sci. Res. **51**, 185 (1993).
[10] J. Zhang, B. Tao, and J. Katz, "Turbulent flow measurement in a square duct with hybrid holographic PIV," Exp. Fluids **23**, 373 (1997).
[11] T. Hori and J. Sakakibara, "High-speed scanning stereoscopic PIV for 3D vorticity measurements in liquids," Meas. Sci. Technol. **15**, 1067 (2004).
[12] W. J. A. Dahm, L. K. Su, and K. B. Southerland, "A scalar imaging velocimetry technique for fully resolved four-dimensional vector velocity field measurements in turbulent flows," Phys. Fluids A **4**, 2191 (1992).
[13] L. K. Su and W. J. A. Dahm, "Scalar imaging velocimetry measurements of the velocity gradient tensor field in turbulent flows. I. Assessment of errors," Phys. Fluids **8**, 1869 (1996).
[14] L. K. Su and W. J. A. Dahm, "Scalar imaging velocimetry measurements of the velocity gradient tensor field in turbulent flows. II. Experimental results," Phys. Fluids **8**, 1883 (1996).
[15] C. J. Kähler and J. Kompenhans, "Multiple plane stereo PIV: Technical realization and fluid-mechanical significance," in Proceedings of the 3rd International Workshop on PIV, Santa Barbara (1999).
[16] C. J. Kähler, M. Stanislas, and J. Kompenhans, "Spatio-temporal flow structure investigation of near-wall turbulence by means of multiplane stereo particle image velocimetry," in Proceedings of the 11th International Symposium on Applications of Laser Technology to Fluid Mechanics, Lisbon, Portugal (2002).
[17] C. J. Kähler, "Investigation of the spatio-temporal flow structure in the buffer region of a turbulent boundary layer by means of multiplane stereo PIV," Exp. Fluids **36**, 114 (2004).
[18] H. Hu, T. Saga, T. Kobayashi, N. Taniguchi, and M. Yasuki, " Dual-plane stereoscopic particle image velocimetry: System set-up and its application on a lobed jet mixing flow," Exp. Fluids **31**, 277 (2001).
[19] B. Ganapathisubramani, E. K. Longmire, I. Marusic, and S. Pothos, "Dual-plane PIV technique to resolve complete velocity gradient tensor in a turbulent boundary layer," in Proceedings of the 12th International Symposium on Applied Laser Technology to Fluid Mechanics, Lisbon, Portugal (2004).
[20] J. A. Mullin and W. J. A. Dahm, "Highly resolved three-dimensional velocity measurments via dual-plane stereo particle image velocimetry (DSPIV) in turbulent flows," 40th AIAA Aerospace Sciences Meeting, AIAA Paper No. 2002-0290 (2002).
[21] J. A. Mullin and W. J. A. Dahm, "Dual-plane stereo PIV (DSPIV) measurements of the velocity gradient tensor field at the small scales of turbulent flows," in Proceedings of the 3rd International Conference on Turbulent Shear Flow Phenomena, Sendai, Japan (2003).
[22] J. A. Mullin and W. J. A. Dahm, "Dual-plane stereo particle image velocimetry (DSPIV) for measuring velocity gradient fields at intermediate and small scales of turbulent flows," Exp. Fluids **38**, 185 (2005).
[23] J. A. Mullin and W. J. A. Dahm, "Dual-plane stereo particle image velocimetry measurements of velocity gradient tensor fields in turbulent shear flow. II. Experimental results," Phys. Fluids **18**, 035102 (2006).
[24] N. J. Lawson and J. Wu, "Three-dimensional particle image velocimetry: Error analysis of stereoscopic techniques," Meas. Sci. Technol. **8**, 894 (1997).
[25] N. J. Lawson and J. Wu, "Three-dimensional particle image velocimetry: experimental error analysis of a digital angular stereoscopic system," Meas. Sci. Technol. **8**, 1455 (1997).
[26] S. Coudert, J. Westerweel, and T. Fournel, "Comparison between asymmetric and symmetric stereoscopic DPIV system," in Proceedings of the 10th International Symposium on Applications of Laser Technology to Fluid Mechanics, Lisbon, Portugal (2000).
[27] R. D. Keane and R. J. Adrian, "Optimization of particle image velocimeters. Part I: Double pulsed systems," Meas. Sci. Technol. **1**, 1202 (1990).
[28] M. Raffel, C. Willert, and J. Kompenhans, *Particle Image Velocimetry: A Practicle Guide* (Springer, New York 1998).
[29] J. A. Mullin, "A study of velocity gradient fields at the intermediate and small scales of turbulent shear flows via dual-plane stereo particle image velocimetry," Ph.D. dissertation, The University of Michigan, Ann Arbor, MI (2004).
[30] S. Biringen, "An experimental investigation of an axisymmetric jet issuing into a coflowing stream," VKI Technical Note 110 (1975).
[31] T. B. Nickels and A. E. Perry, "An experimental and theoretical study of the turbulent coflowing jet." J. Fluid Mech. **309**, 157 (1996).
[32] I. Wygnanski and H. Fiedler, "Some measurements in the self-preserving jet," J. Fluid Mech. **38**, 577 (1969).
[33] H. J. Hussein, W. K. George, and S. P. Capp, "Comparison between hot-wire and burst-mode LDA velocity measurements in a fully developed turbulent jet," AIAA Paper No. 88-0424 (1988).
[34] N. Ninomiya and N. Kasaki, "Measurement of the Reynolds stress budgets in an axisymmetric free jet with the aid of three-dimensional particle tracking velocimetry," in Proceedings of the 9th Symposium Turbulent Shear Flows, Kyoto, Japan (1993).
[35] K. A. Buch and W. J. A. Dahm, "Experimental study of the fine-scale structure of conserved scalar mixing in turbulent shear flows. Part. 1. Sc $\gg 1$," J. Fluid Mech. **317**, 21 (1996).
[36] K. A. Buch and W. J. A. Dahm, "Experimental study of the fine-scale structure of conserved scalar mixing in turbulent shear flows. Part 2. Sc ≈ 1," J. Fluid Mech. **364**, 1 (1998).